

Distinct subnetworks of the thalamic reticular nucleus

<https://doi.org/10.1038/s41586-020-2504-5>

Received: 18 May 2019

Accepted: 9 April 2020

Published online: 22 July 2020

 Check for updates

Yinqing Li^{1,2,3,12}, Violeta G. Lopez-Huerta^{2,3,4,12}, Xian Adiconis^{2,5,12}, Kirsten Levandowski^{2,3}, Soonwook Choi^{2,3}, Sean K. Simmons^{2,5}, Mario A. Arias-Garcia^{2,3,6}, Baolin Guo^{2,3}, Annie Y. Yao^{2,3}, Timothy R. Blosser^{2,3}, Ralf D. Wimmer³, Tomomi Aida^{2,3}, Alexander Atamian^{2,3}, Tina Naik^{2,3}, Xuyun Sun^{3,7}, Dasheng Bi³, Diya Malhotra^{2,3}, Cynthia C. Hession^{2,5}, Reut Shema^{2,3}, Marcos Gomes^{3,8,9}, Taibo Li^{2,3}, Eunjin Hwang¹⁰, Alexandra Krol³, Monika Kowalczyk⁵, João Peça^{8,9,11}, Gang Pan⁷, Michael M. Halassa³, Joshua Z. Levin^{2,5,13}✉, Zhanyan Fu^{2,3,13}✉ & Guoping Feng^{2,3,13}✉

The thalamic reticular nucleus (TRN), the major source of thalamic inhibition, regulates thalamocortical interactions that are critical for sensory processing, attention and cognition^{1–5}. TRN dysfunction has been linked to sensory abnormality, attention deficit and sleep disturbance across multiple neurodevelopmental disorders^{6–9}. However, little is known about the organizational principles that underlie its divergent functions. Here we performed an integrative study linking single-cell molecular and electrophysiological features of the mouse TRN to connectivity and systems-level function. We found that cellular heterogeneity in the TRN is characterized by a transcriptomic gradient of two negatively correlated gene-expression profiles, each containing hundreds of genes. Neurons in the extremes of this transcriptomic gradient express mutually exclusive markers, exhibit core or shell-like anatomical structure and have distinct electrophysiological properties. The two TRN subpopulations make differential connections with the functionally distinct first-order and higher-order thalamic nuclei to form molecularly defined TRN–thalamus subnetworks. Selective perturbation of the two subnetworks *in vivo* revealed their differential role in regulating sleep. In sum, our study provides a comprehensive atlas of TRN neurons at single-cell resolution and links molecularly defined subnetworks to the functional organization of thalamocortical circuits.

The TRN has key roles in sensory processing, arousal and cognition^{1–5}. It consists of a shell of GABAergic neurons, receives inputs from cortical and subcortical regions, and provides the major inhibition to thalamocortical neurons⁴. During sleep, the TRN participates in sleep-rhythm generation, sleep stability and memory consolidation^{10,11}, whereas in active states, TRN neurons contribute to the sensory filtering underlying attention^{3,12}. TRN dysfunction may cause behavioural deficits in disorders including schizophrenia, autism and attention deficit hyperactivity disorder (ADHD)^{6–9}. Despite its importance, little is known about the detailed molecular, cellular and functional organization of the TRN at the single-cell level, a prerequisite for understanding the broad function of thalamocortical circuits.

Though they are often treated as a homogeneous group of GABAergic neurons, an increasing number of studies are suggesting that TRN neurons exhibit heterogeneity in characteristics such as their

molecular and electrophysiological properties, connectivity and function^{13–19}. However, the nature of this heterogeneity and its potential role in shaping thalamocortical circuit function remain unknown. We performed multiscale single-cell analyses to systematically examine the TRN-neuron diversity by integrating transcriptomic profiling, electrophysiological recording, connectivity mapping, *in situ* localization and *in vivo* functional perturbation. We found that TRN neurons cannot be separated into distinct subtypes defined by gene-expression profiles. Rather, TRN neuron heterogeneity is characterized by a transcriptomic gradient of two negatively correlated expression profiles, each containing hundreds of genes. Neurons at the extremes of this transcriptomic gradient can be identified by the near-exclusive expression of a few marker genes including *Spp1* (encoding secreted phosphoprotein 1) and *Ecel1* (encoding endothelin converting enzyme like 1), enabling the characterization of the two subpopulations that we refer to as *Spp1*⁺

¹School of Pharmaceutical Sciences, IDG/McGovern Institute for Brain Research, Center for Synthetic and Systems Biology, Tsinghua University, Beijing, P. R. China. ²The Stanley Center for Psychiatric Research, Broad Institute of MIT and Harvard, Cambridge, MA, USA. ³McGovern Institute for Brain Research and the Department of Brain and Cognitive Sciences, Massachusetts Institute of Technology, Cambridge, MA, USA. ⁴Institute of Cellular Physiology, National Autonomous University of Mexico, Mexico City, Mexico. ⁵Klarman Cell Observatory, Broad Institute of MIT and Harvard, Cambridge, MA, USA. ⁶Faculty of Psychology, National Autonomous University of Mexico, Mexico City, Mexico. ⁷College of Computer Science and Technology, Zhejiang University, Hangzhou, P. R. China. ⁸University of Coimbra, Center for Neuroscience and Cell Biology, Coimbra, Portugal. ⁹University of Coimbra, Institute for Interdisciplinary Research, Coimbra, Portugal. ¹⁰Center for Neuroscience, Korea Institute of Science and Technology, Seoul, South Korea. ¹¹University of Coimbra, Department of Life Sciences, Coimbra, Portugal. ¹²These authors contributed equally: Yinqing Li, Violeta G. Lopez-Huerta, Xian Adiconis. ¹³These authors jointly supervised this work: Joshua Z. Levin, Zhanyan Fu, Guoping Feng. ✉e-mail: jlevin@broadinstitute.org; zfu@broadinstitute.org; fenggg@mit.edu

Article

and *Ecel1*⁺ subpopulations. The two subpopulations exhibit distinct anatomical, physiological and functional features. Notably, the *Spp1*⁺ subpopulation preferentially projected to first order (FO) thalamic nuclei and had a high tendency to generate sustained rebound bursts. By contrast, the *Ecel1*⁺ subpopulation preferentially projected to higher order (HO) nuclei and had a low propensity to generate rebound bursts. Selective perturbation of the two subnetworks in vivo revealed their distinct roles in regulating sleep. Taken together, our study provides a comprehensive atlas of TRN neurons at the single-cell resolution and links systematically identified genetic subnetworks to the functional organization of the mammalian forebrain.

Transcriptomic heterogeneity

We applied single-nucleus RNA sequencing (snRNA-seq) to identify transcriptomic profiles of possible neuronal subtypes. Consistent with previous studies^{20,21}, nearly all TRN neurons expressed *Pvalb*, which showed a high degree of overlap with *Gad2* expression across the entire TRN, as shown by RNA fluorescent in situ hybridization (FISH) (Extended Data Fig. 1). We prepared a single-nucleus cDNA library^{23,24} using microdissected TRN tissue from *Pvalb*-tdTomato transgenic mice²² (Fig. 1a). We analysed the transcriptomes of 1,687 nuclei with an average of 1.3×10^6 mapped reads and a median library complexity of 3,909 genes, in line with previous studies²³.

Clustering analysis identified expected GABAergic (*Gad2*⁺) and non-neuronal cell types as well as glutamatergic neurons (*Slc17a7*⁺), which probably originated from adjacent thalamic regions (Fig. 1b, Extended Data Fig. 2a). Subsequent hierarchical clustering of the GABAergic cells revealed four subpopulations (Extended Data Fig. 2b, c). The predominant cluster was enriched for the inhibitory neuronal marker *Pvalb*, consistent with RNA FISH (Extended Data Fig. 1). This *Pvalb*⁺ cluster (a total of 671 neurons) thus represents inhibitory neurons of the TRN.

t-Distributed stochastic neighbour embedding (*t*-SNE) clustering on the basis of the most variable genes showed no clear subclusters of *Gad2*⁺*Pvalb*⁺ cells, the putative TRN neurons. To capture finer distinctions among closely related TRN neurons, we corrected for batch effects and applied the biSNE clustering algorithm²³ to the *Gad2*⁺*Pvalb*⁺ cells. Notably, biSNE mapped cells to an elongated continuum. Examining the most variable genes showed no obvious demarcation separating the neurons into distinct classes. To assign a cellular transcriptional profile along the continuum precisely, we defined a gradient score for how much the expression of genes deviates relative to the middle of the continuum (Methods). Application of the gradient score revealed a continuous shift in gene expression in TRN neurons (Fig. 1c). Further scoring of the genes by their correlation to the gradient identified two negatively correlated transcriptional profiles (Fig. 1d, e). The first profile was highly expressed on one side of the gradient, and consisted of increased expression of *Spp1* and more than 100 other genes, including *Cacna1i*, encoding the low-voltage-activated T-type calcium channel subunit α -1i, which is important for rebound burst firing of TRN neurons²⁵ (Fig. 1e). The second profile was highly expressed on the other side of the gradient, and consisted of increased expression of *Ecel1* and many other genes, including *Slc6a1*, which encodes a GABA transporter that mediates rapid removal of GABA at the synapse (Fig. 1e). The continuum, which we refer to as a transcriptomic gradient, is characterized mainly by the shift in the number of expressed genes that are specific to the '*Spp1*' profile versus the '*Ecel1*' profile (profile-specific genes) (Fig. 1e, f). Notably, cells that express both *Spp1* and *Ecel1* (referred to as *Spp1*/*Ecel1* double positive (DP)) or express neither (*Spp1*/*Ecel1* double negative (DN)) do not appear to be low quality as a similar number of genes were detected compared with *Spp1*⁺ or *Ecel1*⁺ single-positive cells (hereafter referred to as *Spp1*⁺ or *Ecel1*⁺, respectively) (Extended Data Fig. 3a, b). The DP and DN cells also held intermediate positions along the gradient, suggesting that these cells may be part of a functional range between *Spp1*⁺ and *Ecel1*⁺ profiles

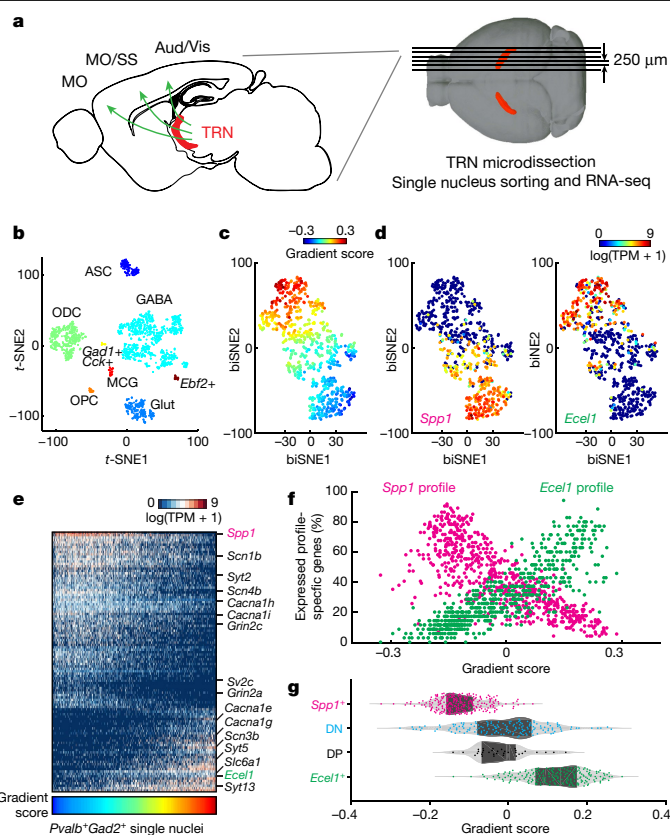


Fig. 1 | snRNA-seq reveals transcriptomic gradient of TRN neurons. **a**, Left, illustration of TRN gating on thalamocortical circuitry and experiments. Green arrows illustrate thalamocortical projection modulated by TRN. MO, motor cortex; SS, somatosensory cortex; Aud, auditory cortex; Vis, visual cortex. Right, TRN tissue is labelled in red (tdTomato). **b**, *t*-SNE shows nuclear clusters, indicated with different colours. ASC, astrocytes; GABA, GABAergic neurons; Glut, glutamatergic neurons; MCG, microglia; ODC, oligodendrocytes; OPC, oligodendrocyte precursor cells. $n = 1,687$ nuclei. **c**, **d**, biSNE embedding of *Gad2*⁺ and *Pvalb*⁺ single nuclei, pseudocoloured by gradient score (**c**) or *Spp1* (left) or *Ecel1* (right) expression (**d**), showing two extremes marked by *Spp1* and *Ecel1*. $n = 671$ nuclei. **e**, Heat map showing *Spp1*- and *Ecel1*-associated transcriptional programs. Some genes relevant to electrophysiological properties are highlighted on the right. Columns show single nuclei and rows are genes. **f**, Scatter plot showing the percentage of *Spp1*- and *Ecel1*-profile-specific genes expressed in individual TRN cells along the transcriptomic gradient. **g**, Distribution of TRN *Spp1*⁺, *Ecel1*⁺ and intermediate DN and DP populations along the transcriptomic gradient.

(Fig. 1e, g). Thus, our data suggest that the molecular diversity in TRN is characterized as a single transcriptomic gradient composed of a combination of two distinct transcription programs marked by highly expressed *Spp1*⁺ or *Ecel1*⁺ profiles.

A shell/core-like distribution

The binarized on-off pattern of *Spp1* and *Ecel1* expression correlates strongly with the transcriptomic gradient (Fig. 1c, d, g, Extended Data Fig. 3a), suggesting that these genes could be used as markers for the two TRN subpopulations. We developed a classification approach to assign neuronal identity along the gradient on the basis of whether *Spp1* or *Ecel1* are expressed. We divided the gradient into three consecutive segments: *Spp1*⁺, DP or DN, and *Ecel1*⁺; cells along the gradient can be classified into one of the three segments with high accuracy (Extended Data Fig. 3c, d),

Thus, to examine the spatial distribution of neurons within the TRN, we used *Spp1* and *Ecel1* as representative markers for the two

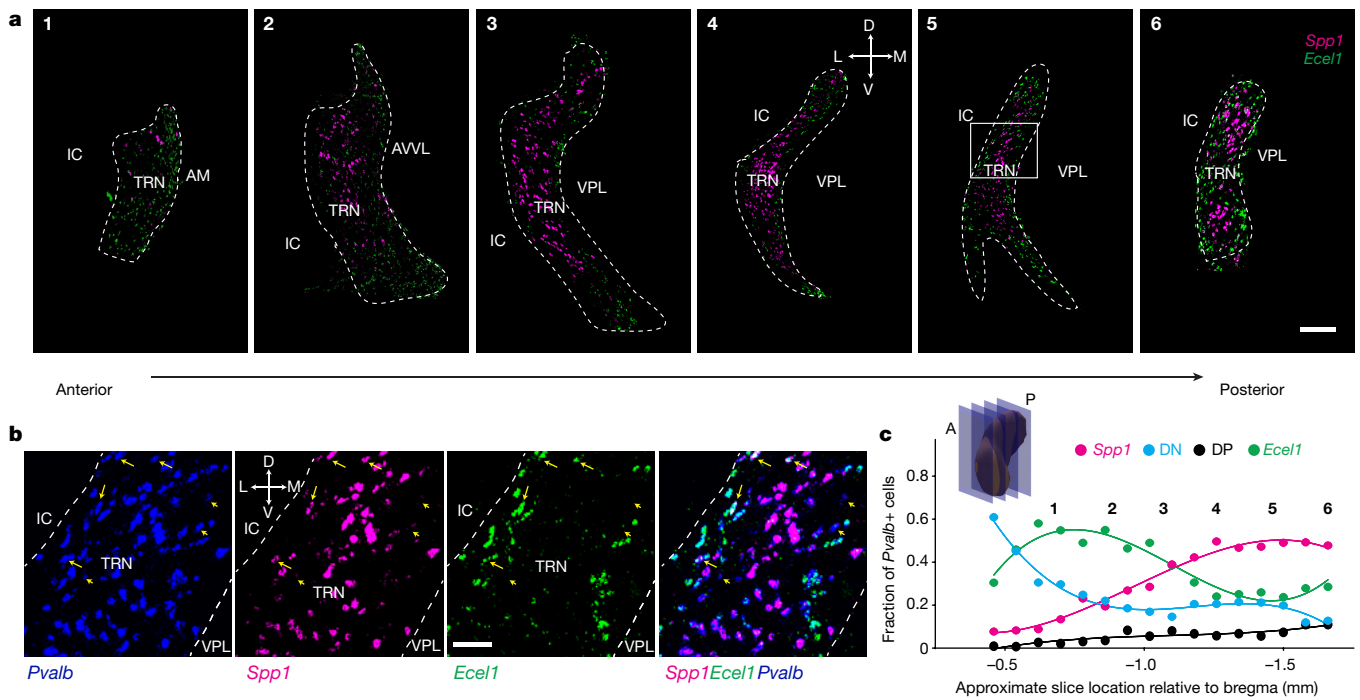


Fig. 2 | *Ecel1*⁺ and *Spp1*⁺ neurons show distinct spatial distribution across the TRN. **a, RNA FISH co-staining in coronal sections. The TRN region is delineated on the basis of the *Pvalb* FISH signal. Scale bar, 200 μ m. D, dorsal; V, ventral; L, lateral; M, medial; AM, anteromedial nucleus; AVVL, anteroventral nucleus; IC, internal capsule; VPL, ventral posterolateral nucleus. $n = 9$**

experiments. **b**, Magnified view of the boxed area in image 5 in **a**. Scale bar, 50 μ m. Arrows show DP neurons; arrowheads show DN neurons. **c**, Fraction of TRN *Pvalb*⁺ cells that are *Spp1*⁺, *Ecel1*⁺, DN and DP, quantified by RNA FISH co-staining in coronal sections along the anterior (A) to posterior (P) axis. Insert, schematic showing orientation of the TRN coronal sections.

subpopulations and performed RNA FISH using *Ecel1*, *Spp1* and *Pvalb* probes. Consistent with snRNA-seq data, *Spp1*⁺ and *Ecel1*⁺ subpopulations exhibited largely non-overlapping expression patterns (Fig. 2). Notably, the *Spp1* and *Ecel1* expression patterns divided TRN into a core (*Spp1*⁺) and shell (*Ecel1*⁺) structure spanning the entire anterior–posterior extent of the TRN, with DP and DN neurons intermingled within the shell and core (Fig. 2a, b, Extended Data Fig. 3e, f). Quantification revealed a gradually increased fraction of *Spp1*⁺ neurons and a reciprocal distribution of *Ecel1*⁺ from anterior to posterior, whereas DP neurons were sparse throughout and DN neurons were most abundant in the anterior part (Fig. 2c).

Hierarchical TRN–thalamic connectivity

Within each functional modality (for example, somatosensory, visual or auditory) thalamic nuclei are categorized into hierarchically distinct FO and HO nuclei on the basis of their principal ‘driver’ inputs^{26,27}. FO nuclei receive and relay peripheral and subcortical sensory information to the cortex, whereas HO nuclei receive their principal driver inputs from cortical layer V and transfer information among functionally related cortical areas^{26–28}.

We next determined whether hierarchically distinct FO and HO thalamic nuclei are innervated by the same or distinct TRN subpopulations. We focused on three main sensory thalamocortical pathways in FO and HO nuclei: visual, somatosensory and auditory. Fluorescent RetroBeads were injected into each thalamic nucleus to retrogradely label TRN and cortical inputs, and RNA FISH was used to determine the molecular identity of labelled TRN neurons (Fig. 3a). The retrograde cortical labelling recapitulated known FO and HO corticothalamic connectivity patterns^{26,28}, confirming the accuracy of our thalamic injection (Extended Data Fig. 4). Notably, we found that the majority of TRN neurons retrogradely labelled by injection in FO nuclei were *Spp1*⁺ (85.7 \pm 3.8%, mean \pm s.e.m.) located in the core region of the TRN. By contrast, most TRN neurons retrogradely labelled from HO nuclei

were *Ecel1*⁺ cells (86.0 \pm 1.3%) located in the shell region of the TRN (Fig. 3b, c). DP and DN TRN neurons did not exhibit an innervation bias (Fig. 3b). These results demonstrate a topographical organization of TRN inputs to hierarchically distinct FO versus HO thalamic nuclei, indicating the existence of specific TRN subnetworks for regulating FO and HO thalamocortical pathways.

Molecular and physiological correlation

We combined whole-cell patch-clamp recordings with snRNA-seq (patch-seq) (Methods) to examine the relation of transcriptional profiles and electrophysiological properties of TRN neurons. We analysed 76 neurons across the entire TRN (Fig. 4a, Extended Data Fig. 5a). For each neuron, we recorded its location and electrophysiological properties. The cell contents were then collected for snRNA-seq. The distribution of transcriptional profiles of these cells was comparable to the continuum gradient in the original snRNA-seq data set, indicating that TRN neuron diversity was adequately sampled (Extended Data Fig. 5b).

TRN neurons are known to display two firing modes, depending on their resting membrane potential: tonic and burst firing. Whereas tonic firing refers to regular sodium spikes at depolarized membrane potentials, burst firing is characterized by repetitive low-threshold T-type Ca²⁺ spikes crowned by high-frequency sodium spike trains elicited at hyperpolarized membrane potentials. This burst firing mode is believed to be critical for the generation and/or maintenance of sleep rhythms and may serve unique functions in information processing^{25,29,30}. We thus analysed rebound burst firing properties of TRN neurons (Fig. 4b). The *Spp1*⁺ subpopulation displayed robust rebound bursting activity (average of 5.5 \pm 2.4 bursts per 5 s; Fig. 4c, d), high spike frequencies within bursts (166.1 \pm 40.2 Hz) and a large post-burst after-hyperpolarization (AHP) (26.5 \pm 8.6 mV; Fig. 4c). By contrast, the *Ecel1*⁺ subpopulation displayed significantly less bursting activity (average of 0.95 \pm 0.8 bursts per 5 s; Fig. 4c, d) and a significantly lower intra-burst spike frequency (86.1 \pm 44.7 Hz) with smaller post-burst

AHP (12.25 ± 9.7 mV; Fig. 4c). DP and DN subpopulations exhibited intermediate firing properties (Fig. 4c, d, Extended Data Fig. 5c). Plotting the key properties of the burst firing showed a distribution pattern similar to that of the transcriptome data (Fig. 4e). Of note, the maximum number of bursts strongly correlated with the molecular gradient score, suggesting that TRN subpopulations have differential molecular mechanisms to generate low-threshold T-type Ca^{2+} spikes, which forms the ionic basis for the rebound burst firing in TRN neurons (Fig. 4f, Extended Data Fig. 5c).

In parallel, we examined the tonic firing by focusing on single action potential (AP) properties including AP threshold and half-width (Aphw), and observed similarly graded changes across TRN subpopulations (Extended Data Fig. 6a, b). *Spp1*⁺ neurons exhibited lower AP threshold and Aphw than *Ecel1*⁺ neurons, suggesting greater excitability, whereas DP and DN subpopulations showed mixed intermediate features. The passive membrane properties, nevertheless, showed little difference among TRN subpopulations (Supplementary Table 1). Moreover, biocytin reconstruction of TRN neurons revealed that neurons with *Ecel1*⁺-like firing pattern had a more complex pattern, with dendritic ramifications extending in nearly all directions. By contrast, *Spp1*⁺-like neurons had shorter total dendritic length (*Spp1*⁺-like, 974 ± 361.8 μm and *Ecel1*⁺-like, 1907 ± 739.3 μm) and a simpler dendritic arborization (number of intersections: *Spp1*⁺-like, 7.5 ± 2.2 and *Ecel1*⁺-like, 14.1 ± 4.6) with a planar discoid-like architecture (Extended Data Fig. 6c–e).

To identify genes contributing to specific neurophysiological properties of TRN neurons, we used a pooled adeno-associated virus (AAV)-mediated CRISPR–Cas9 in vivo knockout approach by targeting distinct groups of genes (Extended Data Figs. 7, 8). We found that knockout of *Kcng1* increased bursting firing in *Ecel1*⁺-like cells, whereas knockout of *Kcnd2* increased rebound bursting in both *Spp1*⁺-like and *Ecel1*⁺-like neurons without modifying other rebound bursting properties (Extended Data Fig. 9). These results suggest that *Kcnd2* and *Kcng1* may normally limit burst firing in TRN neurons (Supplementary Information).

TRN subnetworks in sleep rhythms

During sleep, stereotypical rhythmic activity patterns are observed across the mammalian forebrain³¹ and are thought to contribute to the organization and function of sleep³². It is known that two major patterns, delta and spindle oscillations, depend on reciprocal interactions between thalamus and cortex^{33,34}. In addition, global knockout of *Cacna1i*, the principal low-voltage-activated T-type Ca^{2+} channel in TRN neurons, leads to changes in these rhythms, suggesting that TRN neurons may have specific roles in generating these global forebrain dynamics^{25,35}. As our data revealed a differential propensity of TRN subpopulations to generate low-threshold T-type Ca^{2+} spikes, we investigated whether TRN subpopulations make distinct contributions to sleep rhythms.

To selectively modulate low-threshold Ca^{2+} spikes in the TRN subpopulations, we developed a genetic perturbation approach that uses the γ_6 -subunit of T-type Ca^{2+} channels. Overexpression of γ_6 reduces T-type Ca^{2+} current in vitro by downregulating trafficking of T-type Ca^{2+} channels to the membrane³⁶. Although this subunit is highly expressed in skeletal and cardiac myocytes, it is not expressed in the brain³⁷, and can thus be used to target neurons selectively. We first confirmed the effect of γ_6 on reducing Ca^{2+} currents in brain slices from mice injected in the TRN with lentiviruses containing γ_6 (Extended Data Fig. 10a, b). To target *Spp1*⁺ or *Ecel1*⁺ subpopulations, we injected *cre*-dependent retrograde lentiviruses containing γ_6 fused to mCherry into somatosensory FO ventral posteromedial (VPM; for *Spp1*⁺ neurons) or HO posteromedial (POM; for *Ecel1*⁺ neurons) thalamic nuclei of *Vgat-IRES-cre* mice, which restricts γ_6 expression to the TRN GABAergic neurons that project to the injected thalamic nuclei (Fig. 5a). Overexpression of γ_6 led to a significant decrease in the number of hyperpolarization-evoked

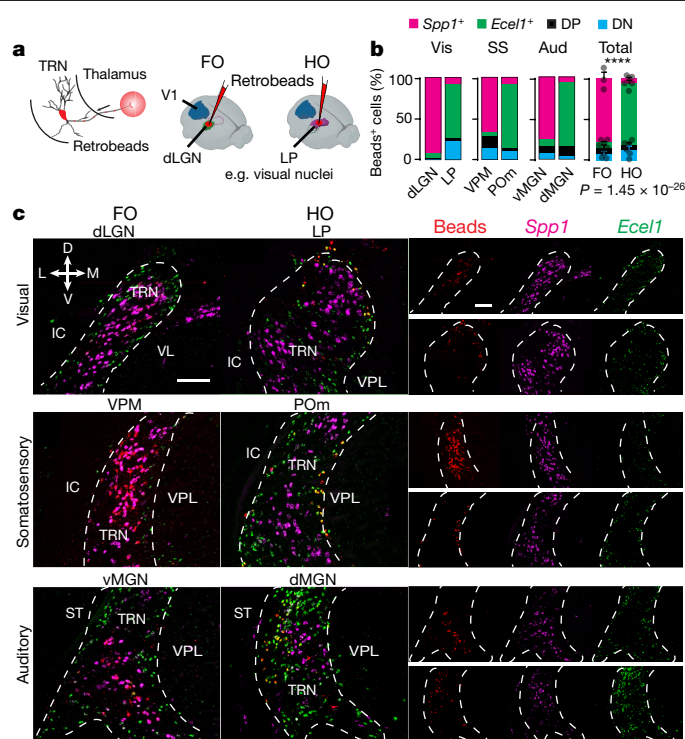


Fig. 3 | Topographical map of TRN-thalamus projections. **a**, Right, schematic illustrating injection of retrograde fluorescent beads (RetroBeads) in FO or HO thalamic nuclei and retrograde tracing to the projecting TRN neurons. Left, an example illustrating tracing from FO (dorsal lateral geniculate nucleus (dLGN)) and HO (lateral-posterior (LP)) visual thalamic nuclei. V1, primary visual cortex. **b**, Percentage of *Spp1*⁺, *Ecel1*⁺, *Spp1*⁺*Ecel1*⁺ and *Spp1*⁻*Ecel1*⁺ cells labelled by RetroBeads traced from injections targeting different thalamic nuclei ($P = 1.45 \times 10^{-26}$; two-sided χ^2 test; mean \pm s.d.). **c**, Retrograde tracing of TRN neurons by projecting to FO thalamic nuclei (dLGN, VPM and ventral medial geniculate (vMGN)) (left) and HO nuclei (LP, POM and dorsal medial geniculate (dMGN)) (right) superimposed with RNA FISH co-staining for *Spp1* and *Ecel1*, showing high overlap of RetroBeads and *Spp1*⁺ staining when FO nuclei were injected and high overlap of RetroBeads and *Ecel1*⁺ when HO nuclei were injected. Separate channels are shown in the columns on the right (top row, injection in FO nuclei; bottom row: injection in HO nuclei). ST, stria terminalis; VL, ventral lateral nucleus. Scale bar, 100 μm . In **b**, **c**, $n = 3$ mice per region.

rebound bursts in both thalamic FO and HO projecting TRN neurons (Fig. 5b, c, Extended Data Fig. 10c–e).

We then performed in vivo electroencephalography (EEG) recordings to determine whether sleep rhythms were affected by specifically reducing the bursting activity of FO- or HO-projecting TRN subpopulations. The γ_6 overexpression in somatosensory FO-projecting TRN neurons, but not in HO-projecting TRN neurons, significantly reduced the power of delta rhythms during non-rapid eye movement (NREM) sleep compared to the control group (Fig. 5d, e). Analysis of spindle oscillations during NREM sleep showed that γ_6 overexpression in somatosensory FO-projecting neurons significantly reduced the number and the length of spindle oscillations (Fig. 5e, f, Extended Data Fig. 10f). By contrast, γ_6 overexpression in HO-projecting subpopulation increased the length of spindle oscillations without changing their numbers (Fig. 5e, f, Extended Data Fig. 10f). Furthermore, we observed a reduction in NREM sleep bouts only in animals expressing γ_6 in FO-projecting TRN neurons but not HO-projecting neurons (Extended Data Fig. 10g, h). Collectively, our data demonstrate that burst firing of TRN neurons mediated by T-type Ca^{2+} channels has a crucial role in sleep spindle generation during NREM sleep, in concert with previous findings^{25,35,38}. Moreover, our data suggest differential roles for the *Spp1*⁺ and *Ecel1*⁺ subpopulations in regulating sleep spindles and sleep bouts.

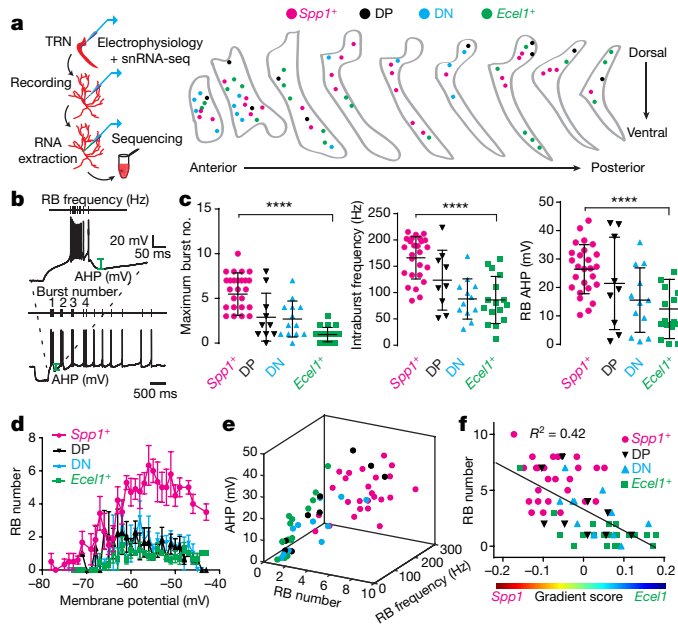


Fig. 4 | *Spp1*⁺ and *Ecel1*⁺ TRN subpopulations show distinct electrophysiological signatures. **a**, Left, schematics of experimental procedure. Right, localization of patch-seq neurons in TRN coronal sections. **b**, Example of the recording protocol used to measure bursting firing; neurons were held at different membrane potentials followed by a hyperpolarizing pulse injection, and traces were quantified in relation to different parameters, including the maximum number of rebound bursts (RBs). **c**, Summary of rebound burst properties ($P = 0.0001$ for all three parameters, two-sided unpaired t -test). Data are presented as individual data points with mean \pm s.d. For maximum rebound burst number, $n = 27$ (*Spp1*⁺), $n = 22$ (*Ecel1*⁺), $n = 10$ (DP) and $n = 13$ (DN); for intraburst frequency and rebound burst AHP, $n = 26$ (*Spp1*⁺), $n = 16$ (*Ecel1*⁺), $n = 9$ (DP) and $n = 12$ (DN) neurons collected from 5 mice. **d**, Number of rebound bursts generated at different membrane potentials. Data are mean \pm s.d. $n = 20$ (*Spp1*⁺), $n = 16$ (*Ecel1*⁺), $n = 10$ (DP) and $n = 13$ (DN) neurons collected from 5 mice. **e**, The 3D plot of rebound bursts number, frequency within the first rebound burst (rbFreq) and AHP, showing the continuous distribution pattern of $n = 26$ (*Spp1*⁺), $n = 16$ (*Ecel1*⁺), $n = 9$ (DP) and $n = 12$ (DN) neurons collected from 5 mice. **f**, Correlation of the gradient score with the maximum number of bursts ($n = 68$ neurons). The line represents linear regression fitting.

Discussion

Our study has generated a comprehensive single-cell-resolution atlas of TRN revealing its cellular heterogeneity in relation to functionally distinct TRN subnetworks. This knowledge will provide a framework for deducing the computational principles of TRN in regulating thalamocortical interactions relevant to sensation, action and cognition.

Contrary to the long-held belief that brain cells are represented by discrete cell types, ours and several other recent reports have found evidence for graded gene expression in multiple brain regions and cell types, though the extent of graded heterogeneity is highly variable. In some cases, a single or a few genes related to developmental cues were found (in retina and cortex^{39,40}), whereas in other cases—similar to the TRN in the present study—tens to hundreds of genes exhibiting continual variation were identified (that is, in the striatum and hippocampal CA1 and CA3)^{23,41–45}. Notably, the continuum of transcriptomic variability in TRN correlates with electrophysiological, connectivity and anatomical organization, suggesting that the transcriptomic gradient may serve to increase heterogeneity underlying a range of cellular properties for wide-range functional tuning. This cellular diversity may facilitate the intrinsic flexibility of TRN to meet the diverse and graded spatial and temporal demands of thalamocortical interactions in the context of sensation, action and cognition.

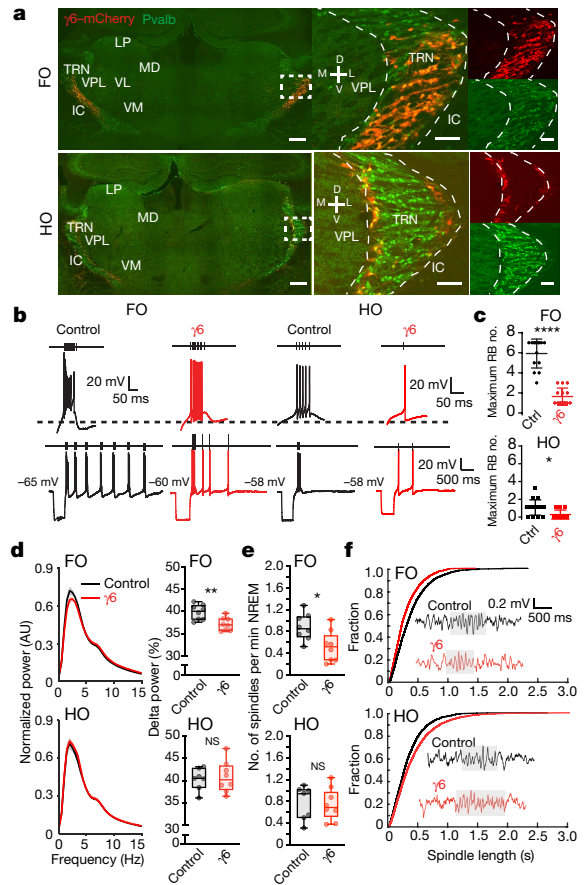


Fig. 5 | Selective perturbation of the firing properties of *Spp1*⁺ or *Ecel1*⁺ neurons in vivo reveals their differential participation in thalamocortical rhythms. **a**, TRN labelled retrogradely with injection in FO (top) and HO (bottom) thalamic nuclei. Left, coronal sections showing TRN (Pvalb⁺) neurons retrogradely-labelled with γ_6 -mCherry (red); boxed areas are magnified (right; merged and single-colour images). Scale bars, 100 μ m. **b**, Traces showing changes of differential firing activity in TRN neurons in response to hyperpolarizing current step injections after injection of γ_6 -AAV in FO and HO thalamic nuclei, which retrogradely preferentially labels *Spp1*⁺ and *Ecel1*⁺ neurons, respectively. **c**, Expression of γ_6 reduced the number of rebound bursts in TRN neurons (FO control, 6.1 ± 1.6 bursts; γ_6 , 1.7 ± 0.8 bursts, $P = 0.0001$; HO control, 1.1 ± 0.26 bursts; γ_6 , 0.3 ± 0.1 bursts; $P = 0.0081$; two-sided unpaired t -test). Data are presented as individual data points with mean \pm s.d. In **a–c**, for FO, $n = 14$ (control) and $n = 18$ (γ_6) neurons from 4 mice; for HO, $n = 12$ (control) and $n = 11$ (γ_6) neurons from 4 mice. **d–f**, Expression of γ_6 in TRN neurons labelled retrogradely from FO led to reduction in the power of delta rhythms (1–4 Hz) (**d**) reduction in spindle density (**e**) and decreased spindle length (**f**), whereas expression of γ_6 in TRN neurons labelled retrogradely from HO led to increased spindle length (**f**). **d**, Left, normalized power spectrum; right, percentage of power in delta rhythm. FO, $P = 0.0045$; HO, $P = 0.75$; two-sided unpaired t -test. In **e**, FO, $P = 0.038$; HO, $P = 0.96$; two-sided Wilcoxon rank-sum test. In **f**, FO, $P = 2 \times 10^{-23}$; HO, $P = 4.5 \times 10^{-13}$; Kolmogorov–Smirnov test. Insert, representative traces of sleep spindles. In **d–f**, for FO, $n = 8$ (control), $n = 8$ (γ_6); for HO $n = 7$ (control), $n = 8$ (γ_6) mice. In box plots, centre points represent median, box edges represent 25th and 75th percentiles, and whiskers show the range of values. NS, not significant.

It remains to be determined whether the transcriptome continuum is a general organizational principle across wide brain regions or a feature specific to integration centres such as the TRN.

From a topographical viewpoint, our results are largely consistent with divided functional reticular modalities based on distinct input–output relationships between cortex and thalamus^{17,46,47}. Within each functional modality, we revealed the distinct spatial distribution of core

(*Spp1*⁺) versus shell (*Ecell*⁺) TRN subpopulations that project to FO and HO thalamic nuclei respectively, providing molecular details for the previous reported ‘slab’ or tier-ordered topographical organization in the somatosensory sector^{17,26,47}. These anatomical types exhibited distinct propensities to generate low-threshold Ca²⁺ spiking characterized by distinctions in rebound burst firing. By targeted ectopic expression of the γ_6 regulatory subunit in these TRN subpopulations, we demonstrated their distinct effects on sleep rhythms (delta and spindle rhythms) *in vivo*.

The TRN has essential roles in sensory processing that require multiple steps and complex computations^{12,48}. Given the distinct electrophysiology and connectivity characteristics of each of the TRN subpopulations, it is likely that these subpopulations mediate different aspects of sensory processing: the first-order projecting *Spp1*⁺ TRN neurons with lasting firing are most probably involved in sensory gating, whereas higher-order projecting *Ecell*⁺ TRN neurons with fast dynamics could be involved in the integration of complex features across modalities or the generation of sensory induced motor signals.

Online content

Any methods, additional references, Nature Research reporting summaries, source data, extended data, supplementary information, acknowledgements, peer review information; details of author contributions and competing interests; and statements of data and code availability are available at <https://doi.org/10.1038/s41586-020-2504-5>.

- Dong, P. et al. A novel cortico-intrathalamic circuit for flight behavior. *Nat. Neurosci.* **22**, 941–949 (2019).
- Halassa, M. M. et al. State-dependent architecture of thalamic reticular subnetworks. *Cell* **158**, 808–821 (2014).
- McAlonan, K., Cavanaugh, J. & Wurtz, R. H. Attentional modulation of thalamic reticular neurons. *J. Neurosci.* **26**, 4444–4450 (2006).
- Pinault, D. The thalamic reticular nucleus: structure, function and concept. *Brain Res. Brain Res. Rev.* **46**, 1–31 (2004).
- Sherman, S. M. & Guillery, R. W. The role of the thalamus in the flow of information to the cortex. *Phil. Trans. R. Soc. Lond. B* **357**, 1695–1708 (2002).
- Ferrarelli, F. & Tononi, G. The thalamic reticular nucleus and schizophrenia. *Schizophr. Bull.* **37**, 306–315 (2011).
- Krol, A., Wimmer, R. D., Halassa, M. M. & Feng, G. Thalamic reticular dysfunction as a circuit endophenotype in neurodevelopmental disorders. *Neuron* **98**, 282–295 (2018).
- Saletin, J. M., Coon, W. G. & Carskadon, M. A. Stage 2 sleep EEG sigma activity and motor learning in childhood ADHD: a pilot study. *J. Clin. Child Adolesc. Psychol.* **46**, 188–197 (2017).
- Stuettgen, P. et al. The thalamic reticular nucleus in schizophrenia and bipolar disorder: role of parvalbumin-expressing neuron networks and oxidative stress. *Mol. Psychiatry* **23**, 2057–2065 (2018).
- Halassa, M. M. et al. Selective optical drive of thalamic reticular nucleus generates thalamic bursts and cortical spindles. *Nat. Neurosci.* **14**, 1118–1120 (2011).
- Latchoumane, C. V., Ngo, H. V., Born, J. & Shin, H. S. Thalamic spindles promote memory formation during sleep through triple phase-locking of cortical, thalamic, and hippocampal rhythms. *Neuron* **95**, 424–435 (2017).
- Wimmer, R. D. et al. Thalamic control of sensory selection in divided attention. *Nature* **526**, 705–709 (2015).
- Brunton, J. & Charpak, S. Heterogeneity of cell firing properties and opioid sensitivity in the thalamic reticular nucleus. *Neuroscience* **78**, 303–307 (1997).
- Clemente-Perez, A. et al. Distinct thalamic reticular cell types differentially modulate normal and pathological cortical rhythms. *Cell Rep.* **19**, 2130–2142 (2017).
- Contreras-Rodríguez, J., González-Soriano, J., Martínez-Sainz, P., Marín-García, P. & Rodríguez-Veiga, E. Neurochemical heterogeneity of the thalamic reticular and perireticular nuclei in developing rabbits: patterns of calbindin expression. *Dev. Brain Res.* **144**, 211–221 (2003).
- Cox, C. L., Huguenard, J. R. & Prince, D. A. Heterogeneous axonal arborizations of rat thalamic reticular neurons in the ventrobasal nucleus. *J. Comp. Neurol.* **366**, 416–430 (1996).
- Lam, Y. W. & Sherman, S. M. Functional organization of the thalamic input to the thalamic reticular nucleus. *J. Neurosci.* **31**, 6791–6799 (2011).
- Lee, S. H., Govindaiah, G. & Cox, C. L. Heterogeneity of firing properties among rat thalamic reticular nucleus neurons. *J. Physiol.* **582**, 195–208 (2007).
- Spreafico, R., de Curtis, M., Frassoni, C. & Avanzini, G. Electrophysiological characteristics of morphologically identified reticular thalamic neurons from rat slices. *Neuroscience* **27**, 629–638 (1988).
- Hou, G., Smith, A. G. & Zhang, Z. W. Lack of intrinsic GABAergic connections in the thalamic reticular nucleus of the mouse. *J. Neurosci.* **36**, 7246–7252 (2016).
- Liu, J. et al. Activation of parvalbumin neurons in the rostro-dorsal sector of the thalamic reticular nucleus promotes sensitivity to pain in mice. *Neuroscience* **366**, 113–123 (2017).
- Kaiser, T., Ting, J. T., Monteiro, P. & Feng, G. Transgenic labeling of parvalbumin-expressing neurons with tdTomato. *Neuroscience* **321**, 236–245 (2016).
- Habib, N. et al. Div-seq: single-nucleus RNA-seq reveals dynamics of rare adult newborn neurons. *Science* **353**, 925–928 (2016).
- Shekhar, K. et al. Comprehensive classification of retinal bipolar neurons by single-cell transcriptomics. *Cell* **166**, 1308–1323 (2016).
- Astori, S. et al. The Ca_v3.3 calcium channel is the major sleep spindle pacemaker in thalamus. *Proc. Natl Acad. Sci. USA* **108**, 13823–13828 (2011).
- Guillery, R. W. Anatomical evidence concerning the role of the thalamus in corticocortical communication: a brief review. *J. Anat.* **187**, 583–592 (1995).
- Sherman, S. M. The thalamus is more than just a relay. *Curr. Opin. Neurobiol.* **17**, 417–422 (2007).
- Ojima, H. Terminal morphology and distribution of corticothalamic fibers originating from layers 5 and 6 of cat primary auditory cortex. *Cereb. Cortex* **4**, 646–663 (1994).
- Lisman, J. E. Bursts as a unit of neural information: making unreliable synapses reliable. *Trends Neurosci.* **20**, 38–43 (1997).
- Steriade, M., McCormick, D. A. & Sejnowski, T. J. Thalamic oscillations in the sleeping and aroused brain. *Science* **262**, 679–685 (1993).
- Huguenard, J. R. & McCormick, D. A. Thalamic synchrony and dynamic regulation of global forebrain oscillations. *Trends Neurosci.* **30**, 350–356 (2007).
- McCormick, D. A. & Bal, T. Sleep and arousal: thalamocortical mechanisms. *Annu. Rev. Neurosci.* **20**, 185–215 (1997).
- Contreras, D. & Steriade, M. Spindle oscillation in cats: the role of corticothalamic feedback in a thalamically generated rhythm. *J. Physiol.* **490**, 159–179 (1996).
- Crunelli, V. et al. Dual function of thalamic low-vigilance state oscillations: rhythm-regulation and plasticity. *Nat. Rev. Neurosci.* **19**, 107–118 (2018).
- Fernandez, L. M. et al. Thalamic reticular control of local sleep in mouse sensory cortex. *eLife* **7**, e39111 (2018).
- Hansen, J. P. et al. Calcium channel γ_6 subunits are unique modulators of low voltage-activated (Cav3.1) calcium current. *J. Mol. Cell. Cardiol.* **37**, 1147–1158 (2004).
- Chu, P. J., Robertson, H. M. & Best, P. M. Calcium channel γ subunits provide insights into the evolution of this gene family. *Gene* **280**, 37–48 (2001).
- Pellegrini, C., Lecci, S., Lüthi, A. & Astori, S. Suppression of sleep spindle rhythmogenesis in mice with deletion of Ca_v3.2 and Ca_v3.3 T-type Ca²⁺ channels. *Sleep* **39**, 875–885 (2016).
- Lo Giudice, Q., Leleu, M., La Manno, G. & Fabre, P. J. Single-cell transcriptional logic of cell-fate specification and axon guidance in early-born retinal neurons. *Development* **146**, dev178103 (2019).
- Sansom, S. N. & Livesey, F. J. Gradients in the brain: the control of the development of form and function in the cerebral cortex. *Cold Spring Harb. Perspect. Biol.* **1**, a002519 (2009).
- Cembrowski, M. S. et al. Spatial gene-expression gradients underlie prominent heterogeneity of CA1 pyramidal neurons. *Neuron* **89**, 351–368 (2016).
- Harris, K. D. et al. Classes and continua of hippocampal CA1 inhibitory neurons revealed by single-cell transcriptomics. *PLoS Biol.* **16**, e2006387 (2018).
- Munoz-Manchado, A. B. et al. Diversity of interneurons in the dorsal striatum revealed by single-cell RNA sequencing and PatchSeq. *Cell Rep.* **24**, 2179–2190 (2018).
- Shah, S., Lubeck, E., Zhou, W. & Cai, L. seqFISH accurately detects transcripts in single cells and reveals robust spatial organization in the hippocampus. *Neuron* **94**, 752–758 (2017).
- Stanley, G., Gokce, O., Malenka, R. C., Sudhof, T. C. & Quake, S. R. Continuous and discrete neuron types of the adult murine striatum. *Neuron* **105**, 688–699 (2019).
- Lee, S. C., Patrick, S. L., Richardson, K. A. & Connors, B. W. Two functionally distinct networks of gap junction-coupled inhibitory neurons in the thalamic reticular nucleus. *J. Neurosci.* **34**, 13170–13182 (2014).
- Pinault, D., Bourassa, J. & Deschênes, M. The axonal arborization of single thalamic reticular neurons in the somatosensory thalamus of the rat. *Eur. J. Neurosci.* **7**, 31–40 (1995).
- Schmitt, L. I. et al. Thalamic amplification of cortical connectivity sustains attentional control. *Nature* **545**, 219–223 (2017).

Publisher's note Springer Nature remains neutral with regard to jurisdictional claims in published maps and institutional affiliations.

© The Author(s), under exclusive licence to Springer Nature Limited 2020

Methods

Data reporting

No statistical methods were used to predetermine sample size. The experiments were not randomized. Unless stated, the investigators were not blinded to allocation during experiments and outcome assessment.

Mice

All experiments were done in accordance with NIH guidelines and approved by the Broad Institute and MIT Institutional Animal Care and Use Committee (CAC 041602419 MIT, CAC 000806141 Broad Institute). Mice were housed with a standard 12 h light/12 h-dark cycle (lights on at 07:00, lights off at 19:00) with ad libitum food and water. All mice used were C57BL/6J background. Animal sample sizes in this study were chosen based on similar previous publications. All mice used in current study were randomly assigned to experimental versus control groups. Experimenters were blinded to genotypes or treatment conditions for data collection and analysis.

Single-nucleus RNA-seq

Dissection of the TRN region. We used a transgenic *Pvalb-tdTomato* mouse line expressing tdTomato in TRN neurons²² and performed fluorescence-aided micro-dissection of tdTomato-positive TRN tissues under a stereo fluorescence microscope. To avoid batch effects due to gender differences, only female mice were included for the whole TRN section series. Female mice at 13–15 weeks of age were deeply anaesthetized with isoflurane followed by cervical dislocation and decapitation for tissue collection. Brains were rapidly removed and placed in ice-cold cutting solution containing (in mM): 194 sucrose, 30 NaCl, 4.5 KCl, 1.2 NaH₂PO₄, 0.2 CaCl₂, 2 MgCl₂, 26 NaHCO₃, and 10 D-(+)-glucose saturated with 95% O₂ and 5% CO₂, pH 7.4, 320–340 mOsm l⁻¹. A sagittal slice (thickness of 250 μm) series covering the whole TRN section was prepared using a slicer (Leica Microsystems, VT1200 S) and placed under a fluorescent stereomicroscope for microdissection. Dissected TRN regions were placed into ice-cold RNAlater (Sigma-Aldrich, R0901) to preserve samples. Afterwards, the samples were transferred to 4 °C overnight followed by storage at –80 °C until further processing. In addition, we collected tissue from thalamus and globus pallidus, which are adjacent to TRN, as controls.

Single nuclei isolation and FACS. We purified nuclei as described²³ with the following modifications. First, we used Vybrant DyeCycle Violet Stain (Thermo Fisher Scientific, V35003) instead of Ruby stain to avoid the spectrum overlapping with tdTomato. Second, in one of the batches, neuronal nuclei were enriched by using NeuN antibody staining⁴⁹. To perform NeuN antibody staining, we incubated purified nuclei in 500 μl phosphate buffered saline (PBS) buffer with 0.5% bovine serum albumin (BSA) (Sigma-Aldrich, A9418) and 0.2 U μl⁻¹ RNase inhibitor (Clontech/TaKaRa, 2313A) at 4 °C for 15 min followed by adding 1 μl anti-NeuN antibody conjugated with Alexa Fluor488 (EMD Millipore, MAB377x) and incubating at 4 °C for another 15 min. We removed the staining buffer after spinning down in 500g for 5 min at 4 °C, re-suspended the nuclei pellet in buffer as described²³ and labelled nuclei with Vybrant DyeCycle Violet Stain. We used an Astrios flow cytometry sorter (Beckman Coulter) to sort one nucleus into each well of 96-well plates containing 5 μl TCL buffer (Qiagen, 1031576) with 1% 2-Mercaptoethanol (b-ME) in each well. We set fluorescence-activated cell sorting (FACS) gating on forward scatter plot, side scatter plot and on fluorescent channels to include only Violet⁺ or Violet⁺ NeuN⁺ (for neuronal nuclei).

Single nucleus RNA library construction and sequencing. Single nucleus RNA library construction was performed as described²⁴. In brief, RNA was first purified using Agencourt RNAClean XP beads (Beckman Coulter, A63987) at 2.2× beads to sample volume ratio. PCR product

was purified using AMPure XP beads (Beckman Coulter, Agencourt AMPure XP, A63880) twice at 0.7X volume ratio and eluted in EB buffer (Qiagen, 19086). Purified cDNA were quality checked on the Agilent 2100 BioAnalyzer with high sensitivity DNA Kit (Agilent, #5067-4626) and quantified using Quant-iT PicoGreen dsDNA Assay Kit (Thermo Fisher Scientific, #P7589) on the EnVision 2104 Multilabel Reader (Perkin Elmer). Sequencing libraries were prepared using a Nextera XT kit (Illumina, FC-131-1024) with 0.075 ng cDNA from each nucleus and 1/4 of the standard reaction volumes. Single nucleus RNA-Seq libraries were sequenced on an Illumina NextSeq 500 with average depth of >1 million reads per nucleus.

Initial processing of sequencing reads. To estimate genome mapping rate, TopHat 2.0.10⁵⁰ was used to align reads to mouse mm10 UCSC genome with default parameters. To estimate gene expression, RSEM v1.2.8⁵¹ was run with default parameters on alignments created by Bowtie2⁵² on UCSC gene annotation. TPM estimates were transformed to log-space by taking log (TPM+1). Genes were considered detected if their transformed expression levels are equal to or above 3 (1.1 in log (TPM+1) scale). A library was removed if it had less than 40% genome mapping rate or less than 1500 detected genes.

Analysis of nuclei clusters. Analysis of nuclei clusters and differential gene expression was performed using biSNE software (https://github.com/yinqingl/nucseq_analysis) according to the instructions as described²³. When clustering TRN *Pvalb*⁺ single nuclei, batch effects were found, which caused data to cluster into three nuclei clusters separated mainly by batches. To correct for this batch effect, the top variant genes within each batch were identified in biSNE analysis, and the identified genes from different batches were pooled. Then, clustering of all TRN *Pvalb*⁺ single nuclei was repeated with these pooled set of top variant genes. To obtain gradient score for the TRN *Pvalb*⁺ neurons, first, pseudo-time was calculated for all TRN *Pvalb*⁺ neurons using biSNE software package with the default parameters. Then, the first 5% and last 5% neurons along the pseudo-time were chosen as two representative populations for the gradient extremes. For each neuron, the median of the Euclidean distance in the PCA space (top 5 PCs) to each member of these two representative populations was calculated and the difference between the medians of the two representative populations was taken as the gradient score.

To assign neuron identities along the gradient, a three-category classifier was constructed using Matlab function 'fitcnb' with weights of *Spp1*⁺, *Ecel1*⁺ samples set to 1 and weights of DP/DN samples set to 2 to normalize sample size. The accuracy of the classifier is estimated using Matlab function 'predict'.

Collection of *Pvalb*⁺ neurons from hippocampus, striatum, somatosensory and motor cortex. Stereotactic viral injections were performed on 8–10 week-old *Pvalb-cre* mice (The Jackson Laboratory, stock 8069). The animals were anaesthetized via isoflurane. One microlitre of high titre AAV1/2 (≈4 × 10¹² Vg ml⁻¹ of pAAV-E F1a-DIO-EGFP-KASH-WPRE-hGH-polyA; a gift from F. Zhang laboratory (MIT)) was injected into dorsal and/or ventral hippocampus, striatum, somatosensory or motor cortex (M2). The Cre-mediated expression of the KASH domain directs the fused GFP protein to the outer nuclear membrane and enables sorting for *Pvalb*⁺ positive nuclei. The corresponding stereotactic coordinates were applied for the four brain regions (hippocampus: AP: –1.7 mm, ML: ±1.0 mm, DV: –1.7 mm; striatum: AP: 0.5 mm, ML: ±2.0 mm, DV: –3.4 mm; somatosensory: AP: –0.7 mm, ML: ±2.8 mm, DV: –1.2 mm; motor cortex: AP: 2.1 mm ML: ±1.5 mm, DV: –1.2 mm). After each injection, the pipette was held in place for 5 min before retraction to prevent leakage. Finally, the incision was sutured and postoperative analgesics (SR-Bupronex, 1 mg kg⁻¹) were administered after the surgery. Three to four weeks later after viral injection, brain tissue from these four regions was dissected into ice-cold RNAlater

Article

followed by the isolation of single nuclei and processing similar to that described in 'Dissection of the TRN region' with the FACS gating set on forward scatter plot, side scatter plot, and on fluorescent channels to include only DAPI⁺GFP⁺ nuclei.

Identification of genes enriched in Pvalb⁺ neurons in TRN compared to other brain regions. First, Smart-seq2 data from non-TRN brain regions (hippocampus, motor cortex (M2), somatosensory cortex and striatum) were processed using RSEM as described in 'Sequencing reads initial processing'. Data from all four tissues were combined into one TPM matrix which was loaded into R and processed with Seurat (v.2.2.0)⁵³. To be consistent with the TRN data, nuclei expressing <1,500 genes were removed. For clustering, variable genes were selected with the FindVariableGenes function (with default parameters, except setting $x.low.cutoff = 1$), while ScaleData function in Seurat package was used to regress out the number of genes per cell. Louvain clustering was performed²⁴ using 50 nearest neighbours and 9 principle components. Clusters were identified based on marker gene expression. Two clusters of Pvalb⁺ inhibitory neurons were used for further analysis.

Second, 10X single cell data from mousebrain.org were processed. Count data and metadata were downloaded from <http://mousebrain.org>⁵³. We extracted a UMI based count matrix consisting of all Pvalb⁺ inhibitory neurons with >500 genes detected. The data were transformed into log counts per million (CPM). We also extracted the clustering information for these cells from the website. Using markers extracted from the Smart-seq2 TRN data (*Six3*, *Sst*, and *Isl1*) two clusters, *DEINHI* and *DEINH2*, were identified as putative TRN Pvalb⁺ inhibitory neurons.

Next, TRN enriched genes were extracted. For the Smart-seq2 data, Pvalb⁺ TRN cells were compared to Pvalb⁺ cells from each of the other 3 tissues with MAST⁵⁴, including the scaled number of genes per cell as a covariate. For the 10X data, the putative Pvalb⁺ TRN cluster was compared to Pvalb⁺ cells from each of the other regions in the dataset, including the scaled number of UMIs per cell as a covariate. We only considered regions that had >50 Pvalb⁺ inhibitory neurons. Here we used the region annotation produced by the mousebrain.org team, except for cells in *DEINHI* and *DEINH2* which were labelled as coming from the TRN. The Pvalb⁺ neurons from the thalamus in the 10X data were also excluded from the analysis, as many of those might be TRN neurons that were clustered with the thalamus cells. In both analyses, we limited ourselves to genes that were detected in at least 10 cells.

We extracted genes that match the following criteria: (a) an FDR adjusted *P* value < 0.05; (b) $\log(\text{fold change}) > \log(2)$ in all comparisons according to MAST⁵⁴; (c) expressed in >40% of TRN cells in both the Smart-Seq2 and mousebrain.org⁵³ data; (d) expressed in <25% of Pvalb⁺ inhibitory neurons in other regions of both datasets.

Disease associated genes. MAST (version 1.05)⁵⁴ was used to find differentially expressed (DE) genes between *Spp1*⁺ cells and *Ecel1*⁺ cells (double positive and double negative cells were excluded). A list of ASD genes was downloaded from the SFARI website (<https://gene.sfari.org/database/human-gene/>) on 25 June 2018⁵⁵. We used all genes with gene scores 1 or 2 (strong/ high confidence genes). A list of Schizophrenia genes was extracted from the recent CLOZUK GWAS⁵⁵. In particular, we took all significant loci that overlapped exactly one gene in either the PGC GWAS or the joint CLOZUK and PGC meta-analysis⁵⁶, and used the associated genes that mapped from human to orthologous mouse genes. In Extended Data Fig. 7d, the plot features all genes from this list with absolute $\log(\text{fold change}) > \log(2)$ and FDR adjusted *P* value < .05 according to MAST. Genes are ordered by $\log(\text{fold change})$, cells ordered as in Extended Data Fig. 7c, and rows are mean centred and scaled by standard deviation, before being plotted using ggplot2.

FISH and image analysis

Multiplex RNA FISH. We used a single molecule fluorescent in situ hybridization (smFISH) method, commercialized as Advanced Cell

Diagnostics RNAScope Fluorescent Multiplex Assay, for FISH experiments. Four and 15 week-old mice were deeply anaesthetized with isoflurane, decapitated, the brains were rapidly dissected out and frozen in blocks using Optimal Cutting Temperature (OCT) compound (Sakura Tissue-Tek, 4583) in an isopropanol/dry ice bath. Serial sections of the samples were cut at 16- μm thickness using a cryostat (Leica Microsystems, CM1850), adhered to SuperFrost Plus microscope slides (Thermo Fisher Scientific, 12-550-15), and stored at -80 °C until use. Samples were immediately fixed in 4% paraformaldehyde for 30 min at 4 °C and stained on the slide according to the Advanced Cell Diagnostics RNAScope Fluorescent Multiplex Assay (ACDBio, 320850) protocol. Samples were then stained for *Pvalb* (ACDBio, 421931), *Spp1* (ACDBio, 435191), *Ecel1* (ACDBio, 475331), *Gad2* (ACDBio, 415071), and *Sst* (ACDBio, 404631) with antisense probes, and mounted with a coverslip using Vectashield hard-set antifade mounting medium with DAPI (Vector Laboratories, H-1500). Z-stack serial images were taken through the whole depth of tissue across the whole TRN on a Nikon Ti Eclipse inverted microscope equipped with an Andor CSU-W1 confocal spinning disc unit and an Andor DU-888 EMCCD together with 20X/0.75 NA air objective lens. Microscope and camera settings were consistent for all imaging procedures.

FISH image analysis and quantification. Identification of the TRN was performed manually and confirmed by the characteristic *Pvalb* expression pattern in this region with reference to the mouse brain atlas. Quantification of cellular colocalization of RNA transcripts was first performed manually using Fiji ImageJ (<https://imagej.net/Fiji>), and then semi-automatically using CellProfiler (<https://cellprofiler.org/>) for each TRN series experiment⁵⁷.

For manual quantification, colocalization was performed on 20X images using the Cell Counter ImageJ plugin. All image Z-stacks were max projected and stitched to obtain the full TRN structure of each sample. In smFISH, the counts of fluorescent puncta reflect the RNA expression level, permitting moderate contrast enhancement without compromising gene-expression assessment. Brightness and contrast were adjusted, and colour was flattened identically across samples. Colocalization of *Pvalb*, *Spp1*, and *Ecel1* FISH experiments, as well as *Pvalb*, *Sst*, and *Gad2* FISH experiments were quantified on a per cell basis, where cells were delineated by DAPI staining. Total Pvalb⁺ neurons, Pvalb⁺ Spp1⁺ neurons, Pvalb⁺ Ecel1⁺ neurons, triple positive Pvalb⁺ Spp1⁺ Ecel1⁺ neurons, and Pvalb⁺ Spp1⁺ Ecel1⁺ neurons were counted.

For CellProfiler semi-automated quantification, a CellProfiler pipeline that involves a series of imaging processing steps to extract cell types was constructed. In brief, for each image, a mask outlining the TRN was drawn manually using signal from the *Pvalb* channel as a guide. Next, the outlines of nuclei (DAPI channel) were identified, following tophat-filter signal enhancement and smoothing, using Otsu thresholding with limits on object size and an algorithm to de-clump groups of tightly packed cells. Similarly, signals from the *Pvalb*, *Spp1*, and *Ecel1* channels were identified using adaptive thresholding after tophat filtering. Finally, *Pvalb* positive cells were identified as those nuclei with a threshold of 30% (by area) co-localization with *Pvalb* signal. *Spp1* positive and *Ecel1* positive cells were identified as nuclei with a threshold of 10% (by area) co-localization with each respective signal. The mean fluorescent intensity for each smFISH channel, which is an approximation for the positive puncta counts normalized by cell size, was obtained for each cell. Complete CellProfiler pipelines for each dataset can be found at <https://cellprofiler.org/>.

To obtain normalized medial-lateral position for TRN cells, TRN left and right boundaries were identified as the leftmost and rightmost Pvalb⁺ neurons at their dorsal-ventral (d-l) positions along the medial-lateral (m-l) axis. The m-l positions of the boundary neurons were smooth-fitted against their d-l positions using Matlab function 'interp1' with 'pchip' kernel. The normalized m-l position of each TRN neuron was calculated as the relative distance to the smoothed left and right boundary at its d-l position, using Matlab function 'interp1'.

Connectivity mapping

Surgery. Three-month-old C57BL/6J mice were anaesthetized with isoflurane and placed in a small animal stereotaxic apparatus (David Kopf Instruments). Animals were injected a volume of 60–80 nl red RetroBeads IX (Lumafluor) using a Nanoject (Drummond Scientific) via glass pipettes with 20–30- μm -diameter tips in different thalamic nuclei (coordinates in Supplementary Table 2). The incision was closed with vetbond and mice recovered on a heat pad in a clean cage. The post-surgery mice were given injected analgesics (SR-Bupronex 1 mg kg⁻¹) every 72 h or as needed, and were allowed to recover for at least 5 days before any experimental procedures. All the experimental mice were group-housed pre and post-surgery.

Cryosectioning and fluorescent staining for retrograde tracing.

Mice were deeply anaesthetized with isoflurane followed by cervical dislocation and decapitation for tissue collection. Mouse brains were removed and placed in cryomolds containing enough fresh OCT medium to cover the sample as described in the section 'Multiplex RNA-FISH'. Sections were cut in a set of 4 rotating series, each containing every one out of four sections. Slides were stored in -80°C until further processing. One series was used to confirm RetroBeads labelling and to select the sections for further processing. In brief, slides were fixed in a standard fixation protocol in 4% paraformaldehyde in PBS (4°C , 15 min) followed by three, 5-min dehydration at room temperature in 50%, 70%, and then 100% ethanol. Once the ethanol was air dried, the samples were stained with Hoechst 33342 (1:1,000) (Thermo Fisher Scientific, H3570) for 15 min at room temperature (RT). After one wash with 1 \times Wash Buffer (ACDBio, USA, 320850), the samples on glass slides were mounted with Fluoromount Aqueous Mounting Media (Sigma-Aldrich, F4680) and left to dry overnight.

RetroBead imaging and counting. Mounted slides were transferred to a microscope equipped with epifluorescence and IR-DIC optics aligned for Kohler illumination. Entire slides were then imaged at $10\times$ for the red RetroBeads (excitation/emission (nm): 530/590), and Hoechst 33342 (excitation/emission (nm): 350/461). The cortical subdivisions were determined according to the Allen Brain Atlas using DAPI channel image. For each cortical subdivision, the RetroBeads were then counted using a custom MATLAB script (https://github.com/yinqingli/image_analysis), which allows normalization of background intensity and pixel counting of fluorescent RetroBeads.

RNA-FISH with RetroBeads

Sections with RetroBeads labelling in the TRN and projection areas were identified as described in 'Cryosectioning and fluorescent staining for retrograde tracing'. Fresh frozen sections, corresponding to the selected sections in the same series of slide-set, were removed from -80°C and fixed in 4% paraformaldehyde in PBS at 4°C for 1 h. FISH for *Ecel1*, *Spp1*, and *Pvalb* expression was performed on selected sections using the RNAscope Fluorescent Multiplex Assay (ACDBio, USA, 320850) according to the manufacturer's instructions. RNAscope probes used were Mm-Spp1-C1 (ACDBio, USA, 435191, NM_001204201.1, region 2-1079), Mm-Ecel1-C3 (ACDBio, USA, 475331-C3, NM_001277925.1, region 879-1992), and Mm-Pvalb-C4 (ACDBio, USA, 421931-C4, NM_013645.3, region 2-885). DAPI (1:1,000) was included in the final wash buffer for nuclear counterstaining. Slides were mounted with coverslips using Fluoromount mounting media.

Confocal imaging. The fluorescent multiplex FISH images were taken as z-stacks on a Nikon Eclipse Ti-E inverted confocal equipped with Andor CSU-W1 spinning disc unit and EMCCD camera (Andor, iXon Ultra 888). Excitation laser lines are 405 nm (DAPI), 488 nm (Alexa Fluor 488), 561 nm (Alexa Fluor 568, RetroBeads), 640 nm (Alexa Fluor 647). Pvalb-C4 was imaged in wide field LED fluorescent using a filter set for

Cy7. Z-stacks were max projected and stitched using ImageJ and Matlab with customized algorithms (https://github.com/yinqingli/image_analysis). ImageJ cell counter was used to manually count RetroBead-labelled cells colocalized with the different FISH probes. Maps of cell localization were generated based on counting density.

Patch-seq

Slice preparation for Patch-Seq. Coronal slices (250 μm) were obtained from *Pvalb-tdTomato* mice at 25–30 p.n. days. Mice were anaesthetized via isoflurane inhalation and perfused transcardially using ice-cold saline containing (in mM): 194 sucrose, 30 NaCl, 4.5 KCl, 1.2 NaH₂PO₄, 0.2 CaCl₂, 2 MgCl₂, 26 NaHCO₃, and 10 D-(+)-glucose saturated with 95% O₂ and 5% CO₂, pH 7.4, 320–340 mOsm l⁻¹. Slices were cut using a slicer (Leica Microsystems, VT1200 S) and then incubated for 10 min in a holding chamber (Scientific System Design, BSK4) at 32°C with regular artificial cerebral spinal fluid (aCSF) containing the following in mM: 136 NaCl, 3.5 KCl, 1 MgCl₂, 2.5 CaCl₂, 26 NaHCO₃ and 11 glucose saturated with 95% O₂ and 5% CO₂, followed by at least one hour recovery at room temperature ($21\text{--}25^{\circ}\text{C}$) before recording.

Electrophysiological recordings and cell content extraction. To obtain electrophysiology and transcriptome data from single neurons, additional modifications were made to the original Patch-seq protocol^{58,59} to improve recording of TRN neurons and RNA recovery. A series of pilot experiments were carried out to test various protocol modifications, including (1) the inclusion of RNase inhibitor in the intracellular patch-clamp solution, (2) silanization of the glass capillaries used for patch-clamping, (3) inclusion of the nucleus during the extraction process, (4) pipette tip size and (5) volume of intracellular solution. These protocols were compared based on electrophysiology recording stability, quality, and cDNA quality measured by BioAnalyzer (Agilent, High Sensitivity DNA Kit, 5067-4626). The following protocol was selected and was used to collect data. Glass capillaries were autoclaved before pulling patch-clamp pipettes, all work surfaces including micromanipulator pieces were thoroughly cleaned with DNA-OFF (Takara, 9036) and RNase Zap (Life Technologies, AM9780) and great care was taken to maintain an RNase-free environment during sample collection. Recording pipettes of 2–4 M Ω resistance were filled with RNase-free intracellular solution containing: 120 mM potassium gluconate, 12 mM KCl, 10 mM HEPES, 1.1 mM EGTA, 4 mM MgATP, 0.3 mM Na₃GTP, and 1 U μl^{-1} recombinant RNase inhibitor (TaKaRa, 2313A), pH about 7.3. To maximize RNA recovery, it was critical to use a small volume of intracellular solution in the patch-clamp pipette (ideally less than 1 μl , but certainly less than 2 μl). RNA was collected at the end of the recording (typically 15–20 min from break-in to RNA extraction) by applying light suction until the cell had visibly shrunken and cell content entered the pipette. The entire nucleus and most of the cytoplasm could often be found entering the pipette, and this was associated with a high yield of cDNA. The contents of the pipette were ejected by applying positive pressure into an RNase-free PCR tube containing 20 μl of TCL buffer with 10% beta-mercaptoethanol and snap frozen on dry ice. The tip of the pipette was broken and left in the same collection tube. The samples were transferred to -80°C until further processing. We used a procedure similar to that described in 'Single nucleus RNA library construction and sequencing', with the modification that all reagents used in Smart-seq2 protocol were scaled up three times, to construct Patch-seq RNA sequencing libraries.

Morphology reconstruction. Brain slices containing biocytin-filled neurons were post-fixed in 4% paraformaldehyde in sodium phosphate-buffer (PBS, pH 7.5) at 4°C . Slices were washed 4 times in PBS and cleared using CUBIC reagent 1^{58,60} (25% urea, 25 wt% *N,N,N',N'*-tetrakis(2-hydroxypropyl) ethylenediamine and 15 wt% polyethylene glycol mono-*p*-isooctylphenyl ether/Triton X-100) for 2 days. After 5–7 washes in PBS, biocytin localization was visualized using

streptavidin-conjugated with Alexa-488 (Thermo Fisher Scientific, S32354). Slices were then re-washed in PBS and submerged in CUBIC reagent 2 (50% sucrose, 25% urea, 10 wt% 2,20,20'-nitrilotriethanol and 0.1% v/v Triton X-100) for further clearing. Post hoc neuroanatomy and neuronal reconstructions were performed using 20x and 60x objectives. Z-stack serial images were acquired on a Nikon Ti Eclipse inverted microscope equipped with an Andor CSU-W1 confocal spinning disc unit and an Andor DU-888 EMCCD camera. Images were collected at 1- μ m z-step intervals. The images were imported into Fiji ImageJ (<https://imagej.net/Fiji>). Individual cells were traced and 3D reconstruction made using the open source Simple Neurite Tracer plugin in the Fiji ImageJ package. Total neurite arbor size and branching was measured within Fiji ImageJ. The skeletonized neuron from Simple Neurite Tracer was used to run Sholl analysis on each traced neuron, with the centre of the cell body as the origin. The Sholl analysis was performed with Fiji ImageJ using the linear method with a sphere separation of 1 μ m and no normalization.

In vivo CRISPR-Cas9 functional genetic screening

Construction of the sgRNA expression vector. The sgRNA expressing vector (AAV:ITR-U6-sgRNA(backbone)-hSyn-EGFP-KASH-WPRE-shortPA-ITR) was constructed based on the AAV:ITR-U6-sgRNA(backbone)-hSyn-Cre-2A-EGFP-KASH-WPRE-shortPA-ITR (pAAV60231) (Addgene, Plasmid 60231)⁶¹. In brief, to remove the Cre from pAAV60231, pAAV60231 was digested by Acc65I and EcoRI (New England Biolabs, R0599 and R3101) and the plasmid backbone was agarose gel purified. EGFP-KASH was PCR amplified from pAAV60231 with primer pair o_BsaI_Acc65I_EGFP_f, o_BsaI_EcoRI_KASH_r (primer sequences in Supplementary Table 6). The amplified product was digested with BsaI (New England Biolabs, R3535) and purified. The sgRNA expressing vector was constructed by ligating the digested backbone and the PCR product using T4 ligase (New England Biolabs, M0202). The sequence of the sgRNA expressing vector was verified by Sanger sequencing.

Selection of the CRISPR-Cas9 targets. We selected targets from three sources, (1) the top differentially expressed genes between *Spp1*⁺ and *Ecel1*⁺ TRN *Pvalb*⁺ neurons; (2) the top differentially expressed genes between *Pvalb*⁺ neurons from TRN and from other brain regions; (3) top risk genes of schizophrenia identified in GWAS studies and de novo mutations found in autism genetic studies. Among the differentially expressed genes, we mainly focused on ion channels and neurotransmitter receptors. A total of 34 genes were chosen and grouped into 7 pools (Supplementary Table 3). Additionally, we added a TRN non-expressing gene *IghE* as a negative control.

Design and cloning of the sgRNA library. Five exon-targeting sgRNAs were designed for each gene using Benchling (<https://benchling.com>). The top 5 sgRNAs with highest predicted on-target efficiency and lowest predicted off-target rate were chosen (<https://benchling.com>) (Supplementary Table 7). Multiple sgRNAs were designed to target a single gene to increase the chance for knockout and to reduce off-target rate. Specifically, for on target, multiplex sgRNA targeting would have higher chance of introducing an exon deletion than a single sgRNA targeting; for off-target, any off-target site would be targeted by no more than one sgRNA whose abundance is reduced to 20% in 5-plex design, leading to reduced off-target rates. The sgRNAs were synthesized individually (Integrated DNA Technologies) and cloned into the sgRNA-expressing AAV vector (AAV:ITR-U6-sgRNA(backbone)-hSyn-EGFP-KASH-WPRE-shortPA-ITR) as previously described⁶¹. In brief, primers (Supplementary Table 6) for each sgRNA were phosphorylated and annealed by T4 Polynucleotide Kinase (New England Biolabs, M0201). The sgRNA library backbone was digested with SapI endonuclease (New England Biolabs, #R0569), and annealed sgRNA inserts were cloned into the backbone by Golden Gate assembly. Then, assembly reactions were transformed into Mix & Go competent *E. coli* (Zymo Research, T3001) according to

the manufacturer's directions. To verify the sgRNA insert sequences, the sgRNA were individually sequenced from the U6 promoter using the U6-fwd primer (Supplementary Table 6).

To make pooled sgRNA libraries, sgRNA targeting selected genes were pooled and concentrated by isopropanol precipitation. Pooled sgRNA libraries were electroporated at 50–100 ng/ μ l using Endura Electrocompetent cells (Lucigen, 60242) according to the manufacturer's instructions, and plated on square assay agar plates with Ampicillin. The bacterial cultures were grown for 14 h and were scraped and collected in LB medium. Midiprep was made using Qiagen Plasmid Plus Midiprep Kit (Qiagen, 12945). The AAV virus serotype AAV2/1 for each pooled sgRNA library was prepared by the Boston Children's Hospital Viral Core.

Surgery for the CRISPR AAV viral injection. Twenty-one- to twenty-five-day-old Cas9 mice⁶² were anaesthetized with isoflurane and placed in a small animal stereotaxic apparatus (David Kopf Instruments). Mice were injected bilaterally a volume of 180 nl of pooled AAV1/2. Two injection points were chosen for each hemisphere to cover most of the TRN at coordinates: AP -0.7, ML 1.65 and DV -3.2/-3.55. The incision was closed with Vetbond and postoperative care was provided as described above. Mice were allowed 10 days of recovery before electrophysiological recordings were performed.

Electrophysiology. Horizontal slices (250 μ m) were obtained from injected mice at 30–35 postnatal days. Mice were anaesthetized via isoflurane inhalation and perfused transcardially with cold saline containing (in mM): 194 sucrose, 30 NaCl, 4.5 KCl, 1.2 NaH₂PO₄, 0.2 CaCl₂, 2 MgCl₂, 26 NaHCO₃, and 10 D-(+)-glucose saturated with 95% O₂ and 5% CO₂, pH = 7.4, 320–340 mOsm l⁻¹. Slices were cut using a slicer (Leica Microsystems, VT1200S) and then incubated for 10 min in a holding chamber (Scientific System Design, BSK4) at 32 °C with regular aCSF containing the following in mM: 136 NaCl, 3.5 KCl, 1 MgCl₂, 2.5 CaCl₂, 26 NaHCO₃ and 11 glucose saturated with 95% O₂ and 5% CO₂, followed by at least one hour recovery at room temperature (21–25 °C) before recording.

We performed whole cell patch-clamp recordings with borosilicate glass pipettes (King Precision Glass, KG33) heat polished to obtain direct current resistances of about 4–6 M Ω . Pipettes were filled with an internal solution containing in mM: 120 K-Gluconate, 2 MgCl₂, 10 HEPES, 0.5 EGTA, 2 Na₂ATP, and 0.2 Na₃GTP. The recordings were made with a microelectrode amplifier with bridge and voltage clamp modes of operation (Molecular Devices, Multiclamp 700B). Cell membrane potential was held at -60 mV, unless otherwise specified. Signals were low-pass-filtered at 2 kHz and sampled at 10–20 kHz with a Digidata 1440A (Molecular Devices), and data were stored on a computer for subsequent off-line analysis. Cells with the series resistance (Rs, typically 8–12 M Ω) changed by >20% were excluded for data analysis. In addition, cells with Rs more than 20 M Ω at any time during the recordings were discarded. AAV1/2 labelled neurons were identified for recordings on the basis of GFP expression visualized with a microscope equipped with GFP filter (Olympus, BX-51WI).

TRN perturbation by γ_6 expression

Construction of γ_6 and control vectors. To construct LV_syn_DIO_gamma6_2a_mCherry, two PCR amplicons DIO-Gamm6-P2A and mCherry-P2A-DIO were amplified from LV_syn_gamma6_2a_mCherry using primer pairs, o_BamHI_DIO_mCherry_f, o_ACCT_p2A_r, and o_ACCT_p2A_f, o_EcoRI_DIO_gamma6_r (Supplementary Table 6). The backbone was constructed by digesting LV_syn_DIO_gamma6_2a_mCherry with BamHI (New England Biolabs, R3136) and EcoRI and gel-purified. The two PCR amplicons and the digested backbone were ligated in a golden gate reaction using BsmBI (Thermo Fisher Scientific, ER0451) and T4 ligase. The constructed plasmid was verified by Sanger sequencing.

To construct LV_syn_DIO_mCherry, amplicon DIO mCherry was cloned from LV_syn_DIO_gamma6_2a_mCherry using primer pair, o_BamHI_DIO_mCherry_f, o_EcoRI_DIO_mCherry_r. The amplicon was combined with the LV_syn_DIO_gamma6_2a_mCherry backbone digested by BamHI and EcoRI in a golden gate reaction using BsmBI and T4 ligase. The constructed plasmid was verified by Sanger sequencing.

Surgery for γ_6 viral injection. Pvalb-Cre or VGat-IRES-Cre mice at 21–25 p.n. days were used for in vitro electrophysiological validation and VGat-IRES-Cre mice of 8–10 weeks old were used for in vivo recordings. Each mouse was deeply anaesthetized with isoflurane and similar procedures as described in ‘Connectivity mapping, Surgery’ section were followed. Retrograde Cre-dependent LV-syn-DIO-gamma6-2a-mCherry (titre 1.6×10^9 IU ml⁻¹, MGH Viral Vector Core) or control LV-syn-DIO-mCherry (2.6×10^9 IU ml⁻¹, MGH Viral Vector Core) lentivirus was FuG-B2 pseudo-typed (pFUGB2) and was injected at the following coordinates for each mouse VPM: AP -1.4, ML 1.5 and DV -3.6; POM: AP -1.6, ML 1.3, DV -3.2. A total volume of 180 nl was injected at each desired depth at the speed of 20 nl per second.

In vitro validation of γ_6 perturbation. In vitro electrophysiological recording were performed similarly as described in ‘In vivo CRISPR-Cas9 functional genetic screening, Electrophysiology’. Additionally, T-type mediated calcium current recordings were performed in voltage clamp mode with a modified aCSF containing (in mM): 120 NaCl, 3 KCl, 20 TEA-Cl, 5 CsCl, 10 HEPES, 14-AP, 2 MgCl₂ and 1 CaCl₂. To ensure calcium current isolation, we used a CsMeSO₄ based internal solution containing in mM: 130 CsMeSO₄, 10 EGTA, 5 MgCl₂, 10 TEA-Cl, 5 Na₂ATP and 10 HEPES.

EEG recordings. Eight- to ten-week-old VGat-IRES-Cre mice were deeply anaesthetized with a 1% to 1.5% isoflurane. After retrograde Cre-dependent LV-syn-DIO-gamma6-2a-mCherry (titre 1.6×10^9 IU ml⁻¹, MGH Viral Vector Core) or control LV-syn-DIO-mCherry (2.6×10^9 IU ml⁻¹, MGH Viral Vector Core) was injected using a nanoinjector, a screw EEG electrode (Pinnacle Technology, 8403) was implanted into the skull above the primary somatosensory cortex, S1 (AP: -1.8 and ML: +3.0 mm) using a stereotaxic device (David Kopf Instruments). A reference electrode was screwed in the occipital region of the skull, and stainless-steel electromyography (EMG) electrodes were placed in the nuchal muscle. All the electrodes were connected to a head-mount (Pinnacle Technology, 8201-SS) and secured by using dental cement. The mice were allowed to recover for at least 2 weeks. Spontaneous EEG/EMG signals were recorded for 48 h with a differential amplifier (Pinnacle Technology, 8200-K1-SL amplifier). All signals were digitized at a sampling frequency of 1,000 Hz, filtered (1–100 Hz bandpass for EEG; 10–1 kHz bandpass for EMG), and acquired using the Sirenia Acquisition program (Pinnacle Technology). Data were analysed offline using Matlab (MathWorks, R2016a). The spectral power was calculated in 0.5-Hz bins (fast Fourier transform with Hamming window) with artefact-free 4-h EEG signals from each mouse. The power for spectral band was normalized in reference to the power of the entire EEG spectrum (1–100 Hz) in each mouse and averaged across all the mice in the same treatment.

Sleep architecture, spindle detection and analysis. Sleep spindles were identified as previously described². In brief, using a semi-automated process, one 12 h light-period of freely moving behaviour was classified for each mouse into three different states based on simultaneous EEG and EMG recordings: wake, non-rapid-eye-movement (NREM) sleep, and rapid-eye-movement (REM) sleep. Wake periods were identified by high EMG activity, and REM sleep was determined by low EMG activity and a high EEG theta/delta power ratio. The remaining epochs were treated as slow wave sleep (SWS). Minimum criteria for Wake and SWS were >16 s and REM was >5 s. NREM sleep bout durations were compared between groups using non-parametric statistics

(Wilcoxon rank-sum and Kolmogorov–Smirnov test). For spindle detection, EEG recordings were filtered within the spindle frequency band (9–15 Hz), and its Hilbert transform (MATLAB function ‘hilbert’) was calculated. The envelope of the signal (1 s smoothing) was used as a basis for spindle detection. A threshold of one standard deviation was applied, and each threshold crossing was initially included. These events were subsequently visually inspected. Visualization was done aided by a time-frequency plot of the EEG signal and was performed blinded to experimental groups. Events <0.5 s were excluded from analysis, as in standard practice⁶³. Spindle count was normalized to time spent in NREM sleep, and spindle duration distributions were compared between groups using non-parametric statistics (Wilcoxon rank-sum and Kolmogorov–Smirnov test, respectively).

Statistical analysis

All data extracted from the analysis of the different experiments were transferred to GraphPad Prism for analysis and graphing, unless otherwise stated. Data are presented as mean \pm s.d. All error bars indicate s.d. unless otherwise stated. A Shapiro–Wilk test was applied to the original data to assess normality of data distribution. Group results were compared by using a two-sided unpaired Student’s *t*-test. The significance level for all tests was $P < 0.05$. Researchers were blinded for the injection sites in the RetroBeads quantifications. Researchers were blinded for the experimental conditions in the EEG recordings and analysis. All electrophysiological recording and data analysis in the first round of CRISPR–Cas9 experiments were performed with researchers blinded to treatment conditions.

Ethics statement

All experiments were done in accordance with NIH guidelines and approved by the Broad Institute and MIT Institutional Animal Care and Use Committee (CAC 041602419 MIT, CAC 000806141 Broad Institute).

Reporting summary

Further information on research design is available in the Nature Research Reporting Summary linked to this paper.

Data availability

Sequencing data for this study is available through the Gene Expression Omnibus GSE145273. All additional data, and plasmids are available from the authors upon reasonable request.

Code availability

Code for the snRNA-seq analyses and the associated *t*-SNE mappings are available at <https://github.com/yinqingl>. Any additional code used is available from the authors upon reasonable request.

49. Krishnaswami, S. R. et al. Using single nuclei for RNA-seq to capture the transcriptome of postmortem neurons. *Nat. Protoc.* **11**, 499–524 (2016).
50. Kim, D. et al. TopHat2: accurate alignment of transcriptomes in the presence of insertions, deletions and gene fusions. *Genome Biol.* **14**, R36 (2013).
51. Li, B. & Dewey, C. N. RSEM: accurate transcript quantification from RNA-seq data with or without a reference genome. *BMC Bioinformatics* **12**, 323 (2011).
52. Langmead, B. & Salzberg, S. L. Fast gapped-read alignment with Bowtie 2. *Nat. Methods* **9**, 357–359 (2012).
53. Zeisel, A. et al. Molecular architecture of the mouse nervous system. *Cell* **174**, 999–1014 (2018).
54. Finak, G. et al. MAST: a flexible statistical framework for assessing transcriptional changes and characterizing heterogeneity in single-cell RNA sequencing data. *Genome Biol.* **16**, 278 (2015).
55. Banerjee-Basu, S. & Packer, A. SFARI Gene: an evolving database for the autism research community. *Dis. Model. Mech.* **3**, 133–135 (2010).
56. Pardiñas, A. F. et al. Common schizophrenia alleles are enriched in mutation-intolerant genes and in regions under strong background selection. *Nat. Genet.* **50**, 381–389 (2018).
57. Kametsky, L. et al. Improved structure, function and compatibility for CellProfiler: modular high-throughput image analysis software. *Bioinformatics* **27**, 1179–1180 (2011).
58. Cadwell, C. R. et al. Electrophysiological, transcriptomic and morphologic profiling of single neurons using Patch-seq. *Nat. Biotechnol.* **34**, 199–203 (2016).

Article

59. Fuzik, J. et al. Integration of electrophysiological recordings with single-cell RNA-seq data identifies neuronal subtypes. *Nat. Biotechnol.* **34**, 175–183 (2016).
60. Susaki, E. A. et al. Advanced CUBIC protocols for whole-brain and whole-body clearing and imaging. *Nat. Protoc.* **10**, 1709–1727 (2015).
61. Joung, J. et al. Genome-scale CRISPR–Cas9 knockout and transcriptional activation screening. *Nat. Protoc.* **12**, 828–863 (2017).
62. Platt, R. J. et al. CRISPR–Cas9 knockin mice for genome editing and cancer modeling. *Cell* **159**, 440–455 (2014).
63. Purcell, S. M. et al. Characterizing sleep spindles in 11,630 individuals from the National Sleep Research Resource. *Nat. Commun.* **8**, 15930 (2017).
64. Hsu, P. D. et al. DNA targeting specificity of RNA-guided Cas9 nucleases. *Nat. Biotechnol.* **31**, 827–832 (2013).

Acknowledgements We thank all members of the G.F., Z.F. and J.Z.L. laboratories for discussions and support; R. Kast for helpful comments on this manuscript; M. Fleishman and M. Palomero-Rivero for technical support; the Broad Flow Cytometry Facility for nucleus sorting; and F. Zhang for CRISPR–Cas9 constructs. The work in the laboratory of G.F. was supported by the Simons Center for the Social Brain at MIT, the Stanley Center for Psychiatric Research at the Broad Institute of MIT and Harvard, Hock E. Tan and K. Lisa Yang Center for Autism Research at MIT, James and Patricia Poitras Center for Psychiatric Disorders Research at MIT, the McGovern Institute for Brain Research at MIT and NIH/NIMH grant R01NS098505, R01NS113245. The work in the laboratory of Z.F. was supported by the Stanley Center for Psychiatric Research at the Broad Institute of MIT and Harvard. The work in the laboratory of J.Z.L. was supported by the Stanley Center for Psychiatric Research and the Klarman Cell Observatory at the Broad Institute of MIT and Harvard. The work in the laboratory of M.M.H. was supported by the Simons Center for the Social Brain at MIT, the Stanley Center for Psychiatric Research at the Broad Institute, the McGovern Institute for

Brain Research at MIT, the Pew Foundation, the Human Frontiers Science Program and NIH grants R01NS098505, R01MH107680. Y.L. was supported by the McGovern–IDG Institute for Brain Research at Tsinghua University.

Author contributions Y.L., V.G.L.-H., J.Z.L., Z.F. and G.F. provided overall design and oversight of the project. snRNA-seq experiments were designed, performed, analysed or supervised by Y.L., V.G.L.-H., X.A., C.C.H., S.K.S. and T.L. A modified protocol for Smart-seq2 library construction was contributed by M.K. Viral injections and collection of non-TRN Pvalb⁺ neuronal nuclei was performed by R.S. and V.G.L.-H. RNA FISH experiments were designed, performed, analysed or supervised by Y.L., K.L., A.Y.Y., T.R.B., A.A., M.G. and J.P. EEG recording and analyses were designed and performed by S.C., R.D.W., V.G.L.-H., B.G., T.N., X.S., D.B., E.H., G.P. and M.M.H. Electrophysiology, patch-seq and morphology experiments were designed, performed, analysed or supervised by V.G.L.-H., M.A.A.-G., Y.L. and Z.F. Retrograde tracing experiments were performed by V.G.L.-H., Y.L., A.Y.Y., A.A., K.L. and A.K. CRISPR-knockout experiments were designed and performed by Y.L., V.G.L.-H., X.A., T.A., A.Y.Y., A.A. and D.M. The manuscript was written by Y.L., V.G.L.-H., Z.F., G.F., J.Z.L. and M.M.H. with inputs from all authors.

Competing interests The authors declare no competing interests.

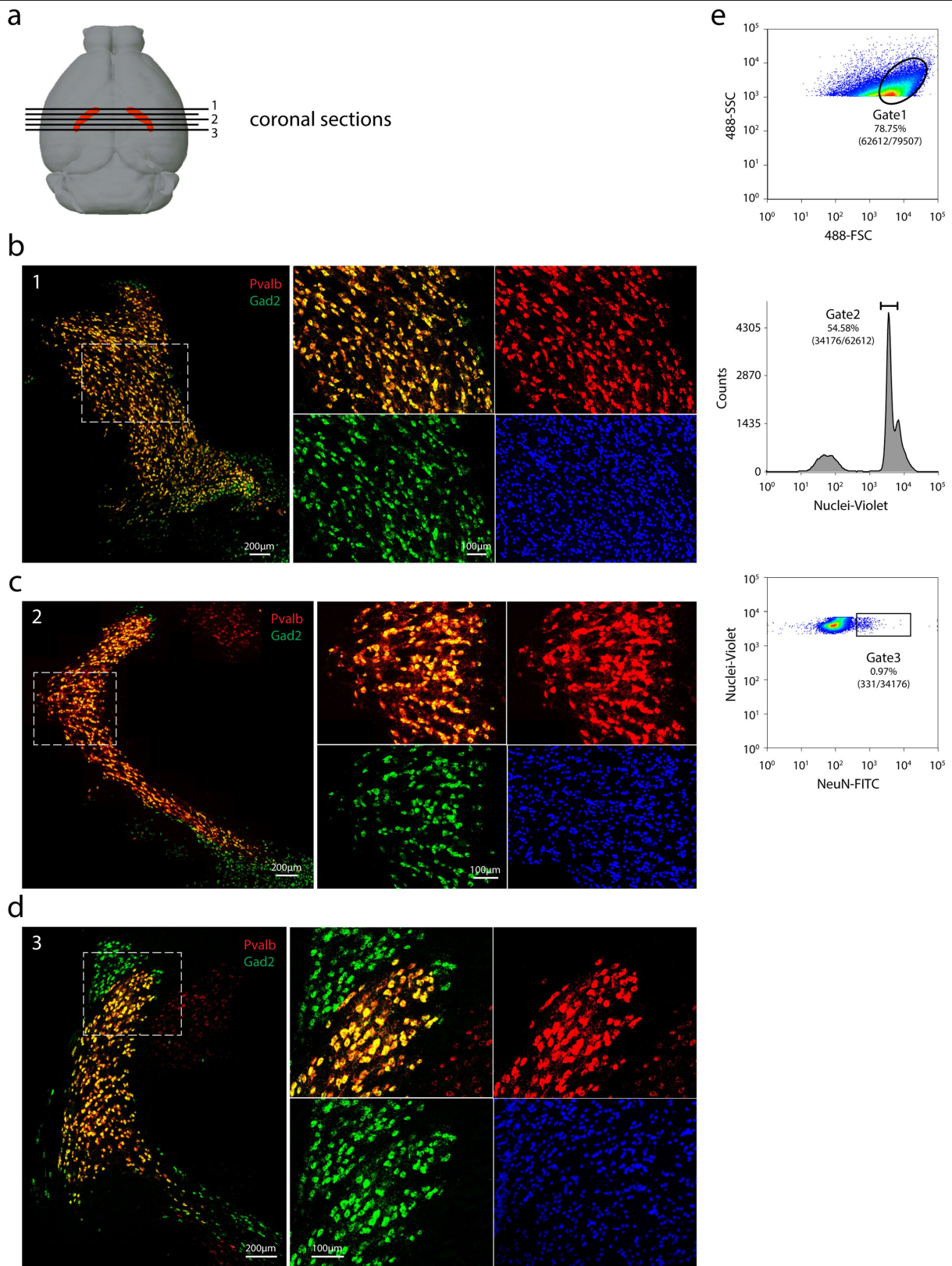
Additional information

Supplementary information is available for this paper at <https://doi.org/10.1038/s41586-020-2504-5>.

Correspondence and requests for materials should be addressed to J.Z.L., Z.F. or G.F.

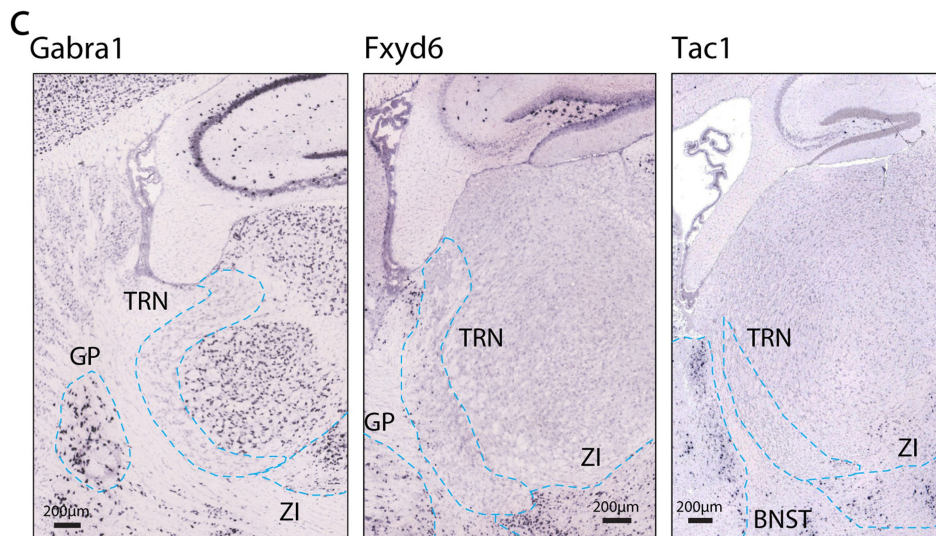
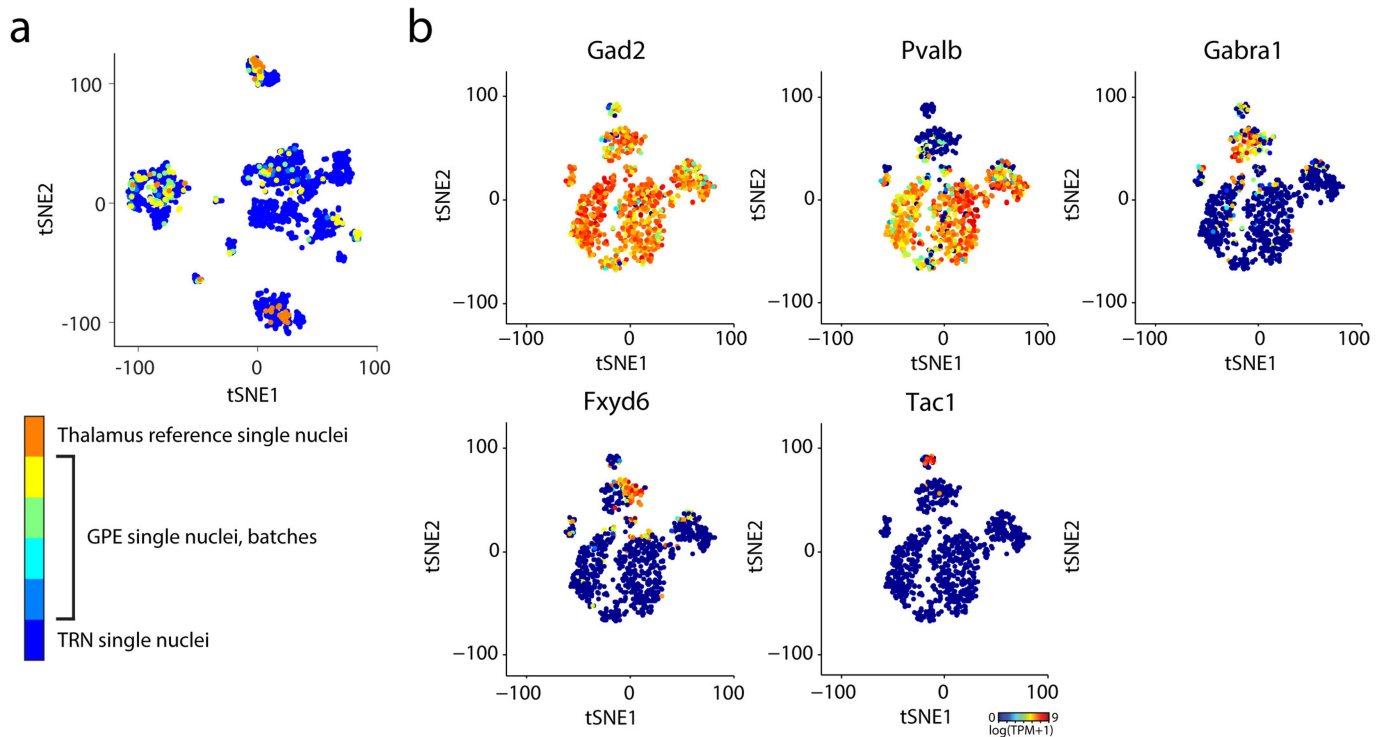
Peer review information *Nature* thanks Ed S. Lein, Karel Svoboda and the other, anonymous, reviewer(s) for their contribution to the peer review of this work.

Reprints and permissions information is available at <http://www.nature.com/reprints>.



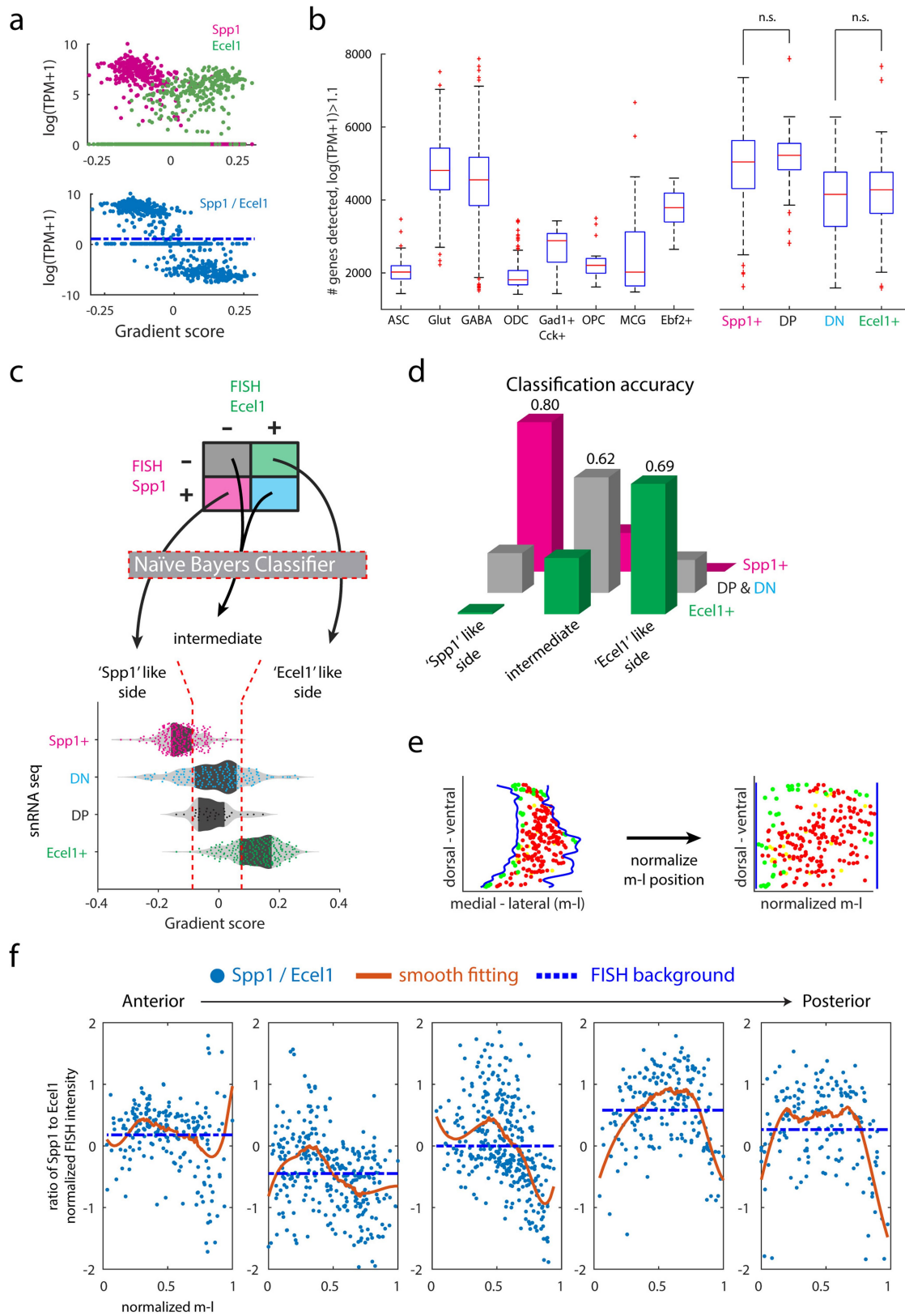
Extended Data Fig. 1 | Expression patterns of *Gad2* and *Pvalb* across TRN.
a, Schematic of positions of coronal sections shown along the anterior to posterior axis (indicated by numbers). **b–d**, RNA-FISH co-staining of *Gad2* and *Pvalb* in anterior (**b**), medial (**c**), and posterior (**d**) coronal sections. For each

position: Left: overview of the RNA-FISH co-staining in TRN; Right: Zoom-in view of the boxed area in the left panel. For **b–d**, repeated with $n = 2$.
e, Representative FACS plot showing gating strategy used in sorting single nuclei for RNA sequencing. Repeated with $n = 53$ plate-based sorting.



Extended Data Fig. 2 | Identification of *Gad2*⁺ cell types. **a**, *t*-SNE embedding of 1,687 single nuclei as in Fig. 1a. Single nuclei are coloured by dissection sources as indicated by the colour bar on the right. Different batches of dissections from the external part of globus pallidus (GPE) are coloured differently. $n = 1,687$ nuclei. **b**, *t*-SNE embedding of nuclei showing expression levels (pseudo-colour) of marker genes for each cluster. The three small

clusters exhibiting markedly less *Pvalb* expression, but enriched with a combination of markers including *Gabra1*, *Fxyd6*, *Tac1*. $n = 868$ nuclei. **c**, ISH image in sagittal view of selected markers shown in **b**. Images obtained from Allen Brain Atlas (<https://portal.brain-map.org/>). Dashed lines indicate boundaries of TRN and the neighbouring GABAergic nuclei. GP: globus pallidus; ZI: zona incerta; BNST: bed nucleus of the stria terminalis.

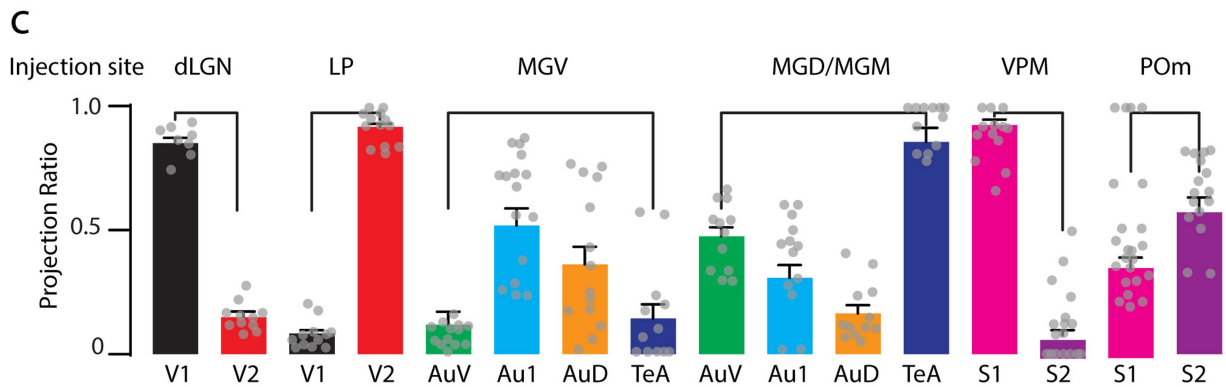
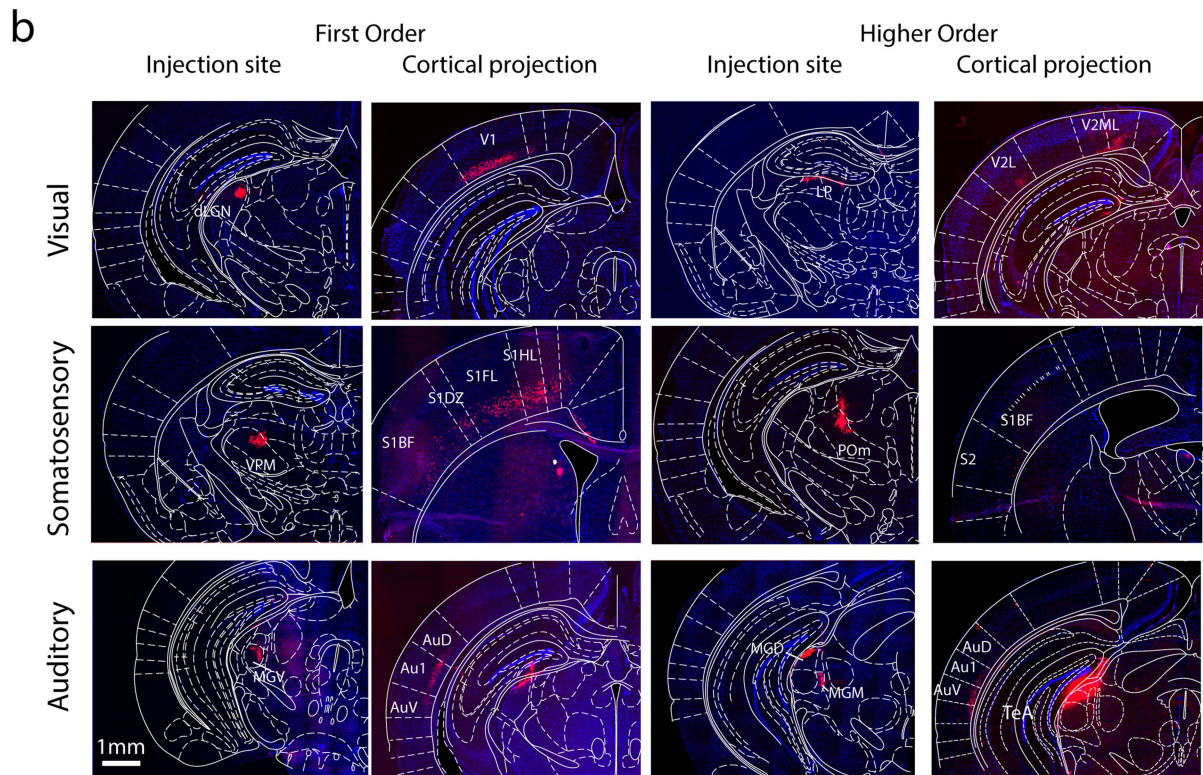
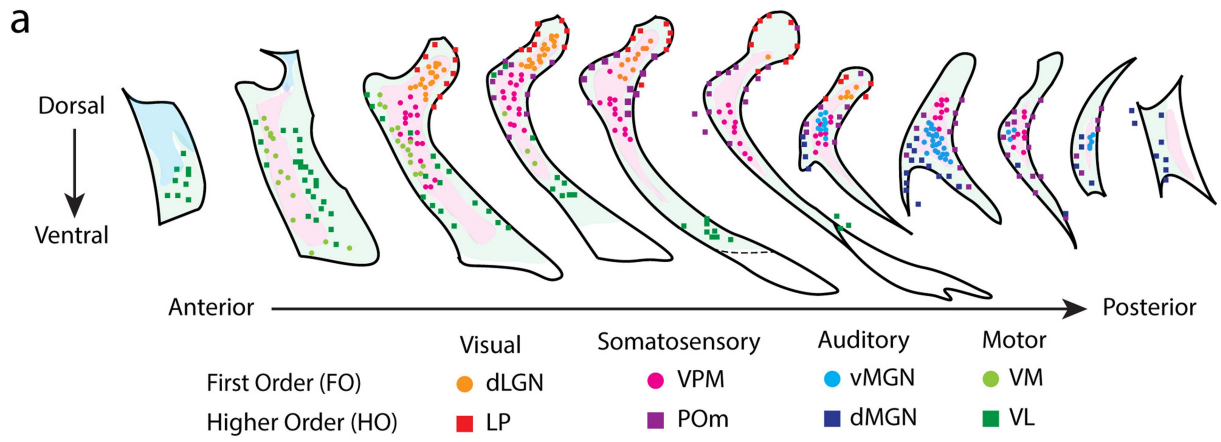


Extended Data Fig. 3 | See next page for caption.

Article

Extended Data Fig. 3 | Binarized expression pattern of *Spp1* and *Ecel1* represents transcriptomic gradient. **a**, Expression levels of *Spp1* and *Ecel1* (top) and $\log(Spp1/Ecel1)$ (bottom) in individual cells along the transcriptomic gradient, showing binary pattern of *Spp1* and *Ecel1* correlated with the gradient score. **b**, Number of genes detected for the major cell types and TRN subpopulations, showing that the *Spp1*⁺*Ecel1*⁺ (DP) and *Spp1*⁺*Ecel1*⁻ (DN) are of quality comparable to other cell populations. $n_{ASC} = 124$, $n_{Glut} = 226$, $n_{GABA} = 868$, $n_{ODC} = 388$, $n_{Gad1}^{+} cck^{+} = 9$, $n_{OPC} = 23$, $n_{MCG} = 28$, $n_{Ebf2}^{+} = 21$ nuclei. Between *Spp1*⁺ and DP, $P = 0.1787$; DN and *Ecel1*⁺, $P = 0.2897$, two-sided ranksum test. n.s.: not significant. No adjustment for multiple testing was applicable. Box plots shows 25th, 50th, 75th percentiles, and the whiskers extend to the most extreme data points, '+' are taken as outliers. **c**, Schematics of naive Bayes classifiers to assign *Spp1*⁺, *Ecel1*⁺, DP and DN neurons into segments of the transcriptomic gradient. **d**, Classification accuracy of the naive Bayes classifiers. Shown are the

probability of assigning *Spp1*⁺ to 'Spp1' segment, DP and DN neurons to the intermediate segment, and *Ecel1*⁺ to 'Ecel1' segment, respectively. $n = 671$ nuclei total, $n_{Spp1}^{+} = 264$, $n_{DP+DN} = 195$, $n_{Ecel1}^{+} = 212$ neurons. **e**, Schematics for normalization of medial-lateral position of individual neurons in FISH images. Blue line: TRN boundary; Red dots: *Pvalb*⁺*Spp1*⁺ neurons; Green dots: *Pvalb*⁺*Ecel1*⁺ neurons; Yellow dots: DP neurons; DN are not shown in the schematics. **f**, Scatter plots showing $\log(Spp1/Ecel1)$ in individual *Pvalb*⁺ neurons at normalized medial-lateral position in selected tFISH images along anterior to posterior TRN, corresponding to Fig. 2c. m-l: medial-lateral position; Blue dots: individual cells; Solid red line: smooth fitting of blue data points, showing inverted-'U' shape; Dashed blue line: mean of blue data points, indicating the difference in the FISH background of *Spp1* and *Ecel1* channel in different images.

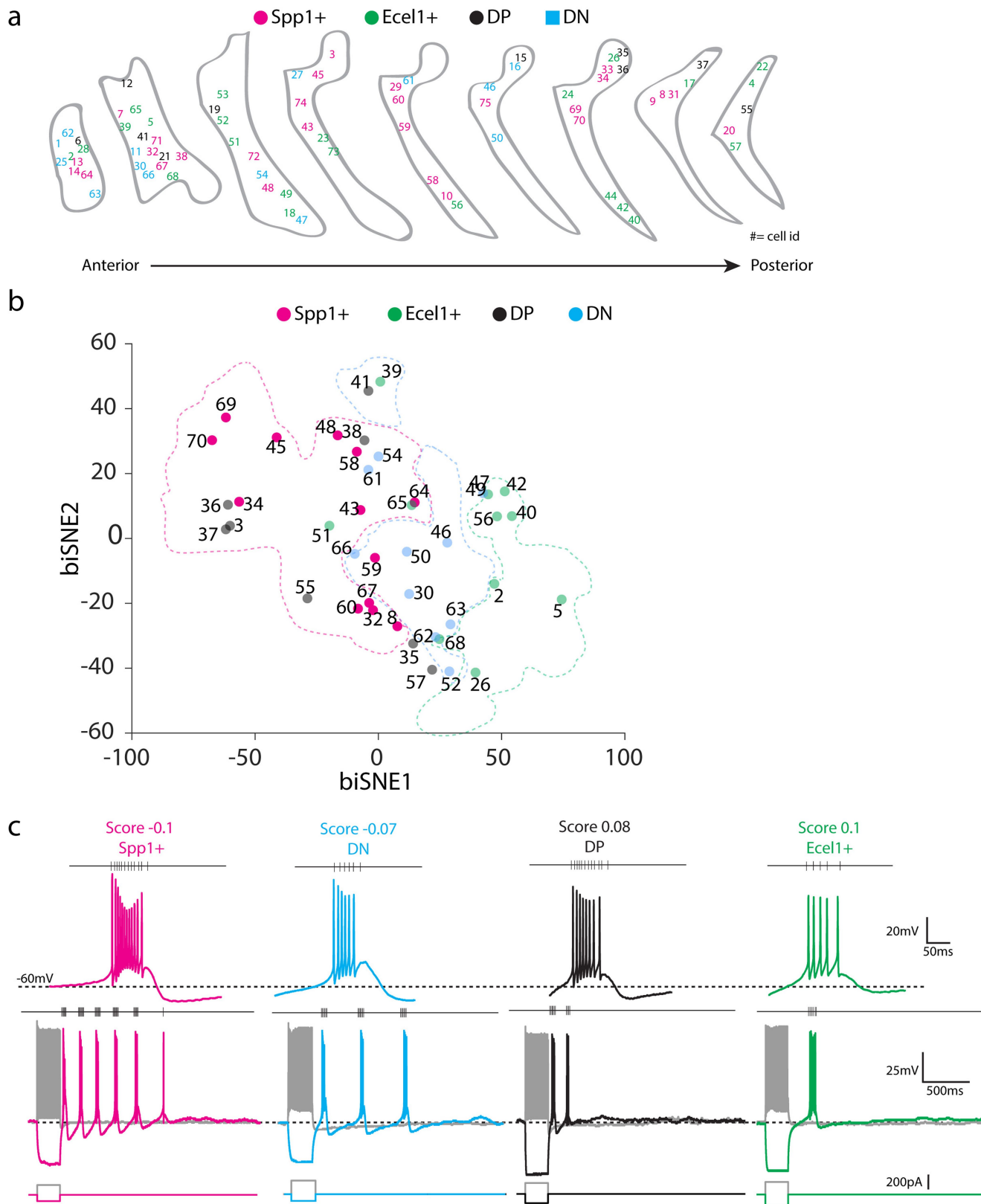


Extended Data Fig. 4 | See next page for caption.

Article

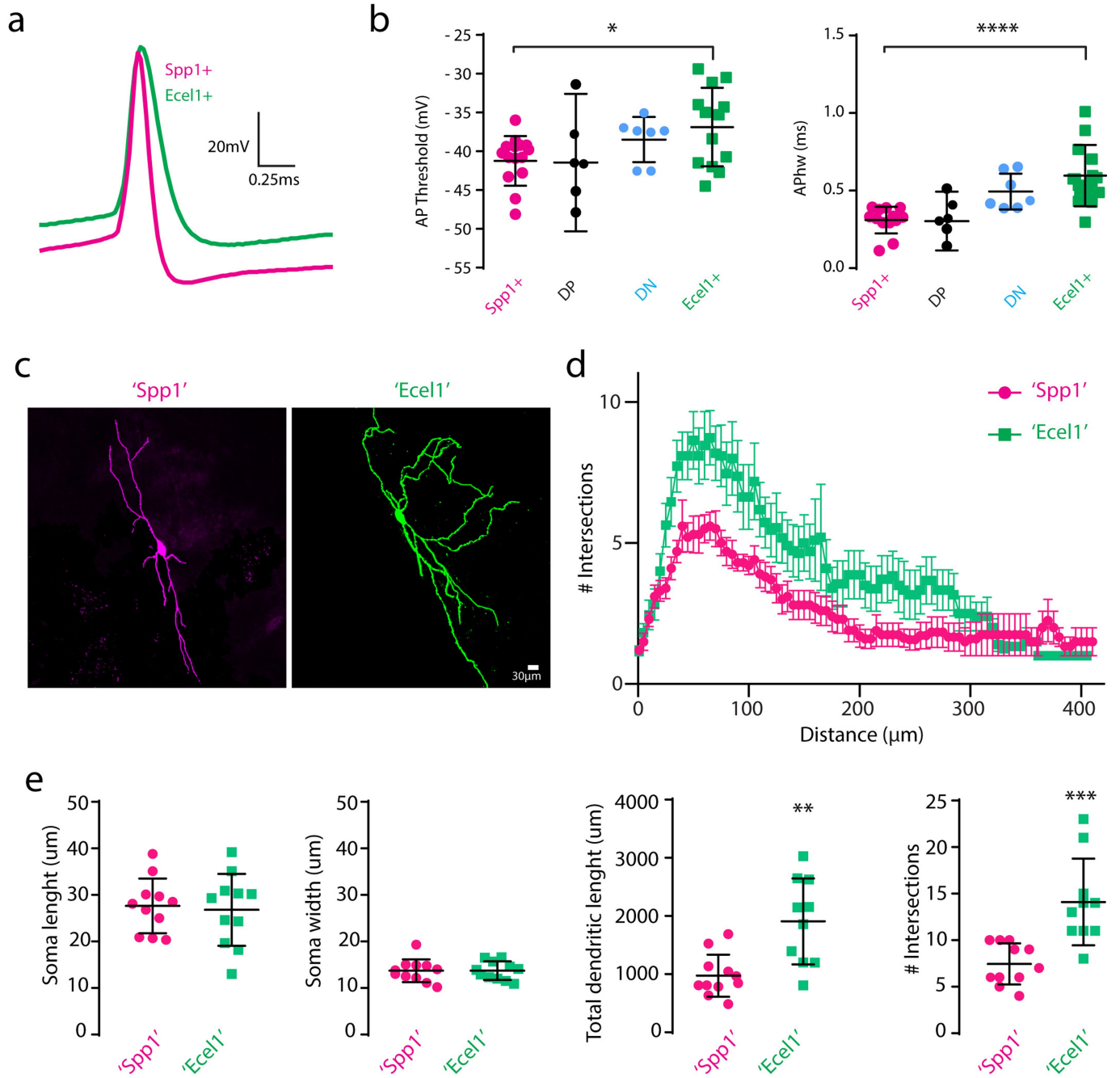
Extended Data Fig. 4 | Injection sites in distinct thalamic relay nuclei and corresponding cortical projections. **a**, The positions of retrogradely labelled neurons traced from different thalamic relay nuclei indicated by different colours are shown in the coronal view of TRN section series arranged from anterior to posterior. The light green and the magenta shaded areas indicate the distribution of typical *Ecel1⁺* and *Spp1⁺* neurons, respectively. VPM, ventral posterior medial; dLGN, lateral geniculate nucleus (dorsal part); POM, posterior-medial; LP, lateral posterior-lateral part; dMGN, medial geniculate-dorsal part; vMGN, medial geniculate-ventral part; VM, ventromedial; VL, ventrolateral. *n* = 3 mice per region. **b**, Panoramic view of coronal sections showing the injection sites and cortical projection for each FO and HO thalamic nuclei. V1: primary visual cortex; V2L: secondary visual cortex lateral part; V2ML: secondary visual cortex medial-lateral part; S1BF: primary

somatosensory cortex barrel field; S1DZ: primary somatosensory cortex dysgranular zones; S1FL: primary somatosensory cortex forelimb; S1HL: primary somatosensory cortex hindlimb; S2: secondary somatosensory cortex; AuV: secondary auditory cortex ventral area; AuI: primary auditory cortex; AuD: secondary auditory cortex dorsal area; MGD: medial geniculate nuclei dorsal part; MGM: medial geniculate nuclei medial part; TeA: temporal cortex, association area. *n* = 3 mice per region. **c**, Quantification of the projection ratio between the primary and higher-order secondary/tertiary cortical areas for different thalamic injection sites. $n_{\text{dLGN}} = 12$ slices/2 mice, $n_{\text{LP}} = 12$ slices/2 mice, $n_{\text{MGN}} = 15$ slices/2 mice, $n_{\text{MGD/MGM}} = 12$ slices/2 mice, $n_{\text{VPM}} = 12$ slices/2 mice, $n_{\text{POM}} = 12$ slices/2 mice. Bars represent mean \pm s.e.m. and raw data points.



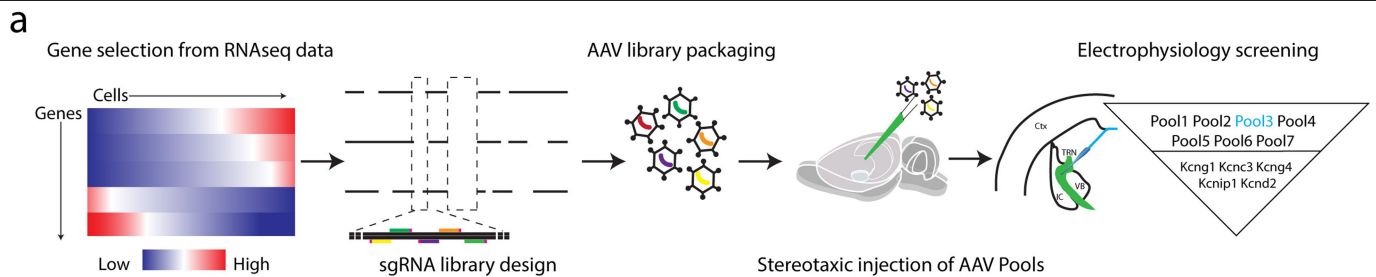
Extended Data Fig. 5 | Distribution of TRN neurons according to molecular gradient score. a, The anatomical distribution of Patch-seq recorded neurons in coronal sections of TRN along the anterior-posterior axis. The cells were labelled with different coloured numbers as indicated (*Spp1*⁺, magenta, *Ecel1*⁺, green, DP, black and DN, blue). Numbers indicate cell ID. Shown are $n = 76$ cells/5 mice, data collected by 2 experimenters. **b,** biSNE embedding of the collected TRN neurons for Patch-seq showing molecular gradient pattern with *Spp1*⁺ (magenta), *Ecel1*⁺ (green), and the intermediate sub-populations DP (black) and

DN (blue). Shown are subset of neurons from a batch of $n = 68$ neurons/5 mice. **c,** Representative voltage changes in response to hyperpolarizing current step injections. *Spp1*⁺ neurons (magenta) show robust rebound burst firings elicited by hyperpolarization with high firing frequencies within a burst. When a similar protocol is applied, most of the *Ecel1*⁺ neurons (green) show only one rebound burst with lower firing frequencies within a burst than *Spp1*⁺ neurons. DN (blue) and DP (black) neurons present intermediate properties. $n_{Ecel1^+} = 15$, $n_{Spp1^+} = 29$, $n_{DN} = 9$, $n_{DP} = 10$ neurons.



Extended Data Fig. 6 | TRN neurons exhibit difference in action potential properties and morphology. a, Zoom-in view of a representative single action potential traces of *Spp1*⁺ and *Ecel1*⁺ neurons. **b**, Summary of action potential (AP) threshold ($P=0.015$, two-sided unpaired *t*-test) and half-width of AP (APhw) ($P=7.08 \times 10^{-5}$, two-sided unpaired *t*-test). For **a**, **b**, $n_{Spp1} = 12$, $n_{Ecel1} = 13$, $n_{DP} = 6$, $n_{DN} = 7$ neurons from 5 mice. Plots represent mean \pm s.d. and raw data

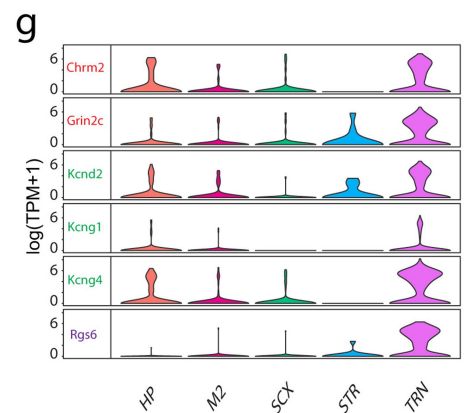
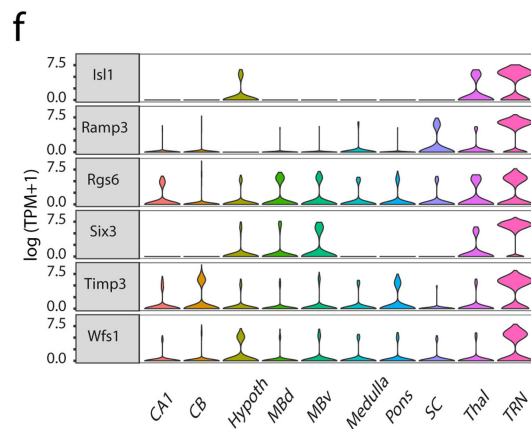
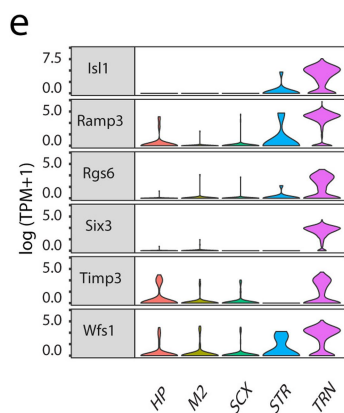
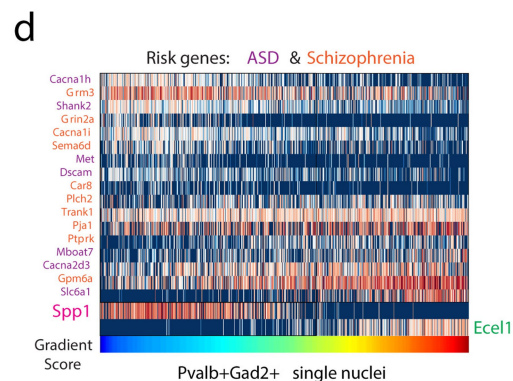
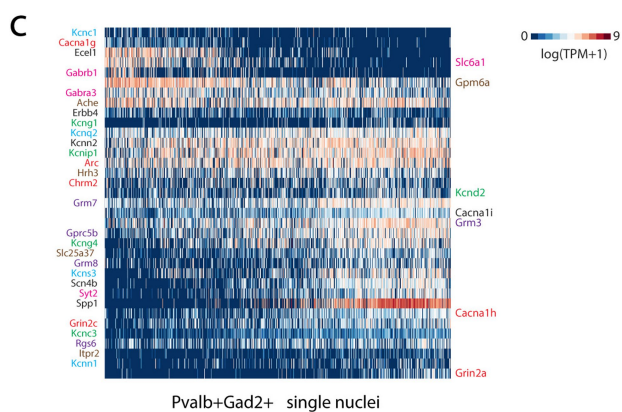
points. **c**, Example of *Spp1*⁺ like ('*Spp1*') (magenta) and *Ecel1*⁺ like ('*Ecel1*') (green) neuron morphology. **d**, Sholl analysis of the dendritic complexity. **e**, Summary of the soma length and width, total dendritic length and maximum number of intersections in *Spp1*⁺ like ('*Spp1*') and *Ecel1*⁺ like ('*Ecel1*') neurons (Mean \pm s.d. Dendritic length, $P=0.0014$. Number of intersections, $P=0.0004$, two-sided unpaired *t*-test). For **c**–**e**, $n_{Spp1} = 11$ neurons/4 mice, $n_{Ecel1} = 10$ neurons/4 mice.



b

Control Ighe	Pool#2 Kcnc2, Kcnc1, Kcnn1, Kcns3	Pool#4 Slc6a1*, Gabrb1, Gabra3, Syt2	Pool#6 Grm3*, Grm7, Grm8, Rgs6, Gprc5b
Pool#1 Kcnn2, Cacna11*, Scn4b, Erbb4	Pool#3 Kcng1 Δ , Kcnc3, Kcng4 Δ , Kcnp1, Kcnd2* Δ	Pool#5 Cacna1g, Cacna1h*, Arc, Grin2a*, Grin2c, Chrm2	Pool#7 Slc25a37, Hrh3, Gpm6a*, Ache, Itpr2

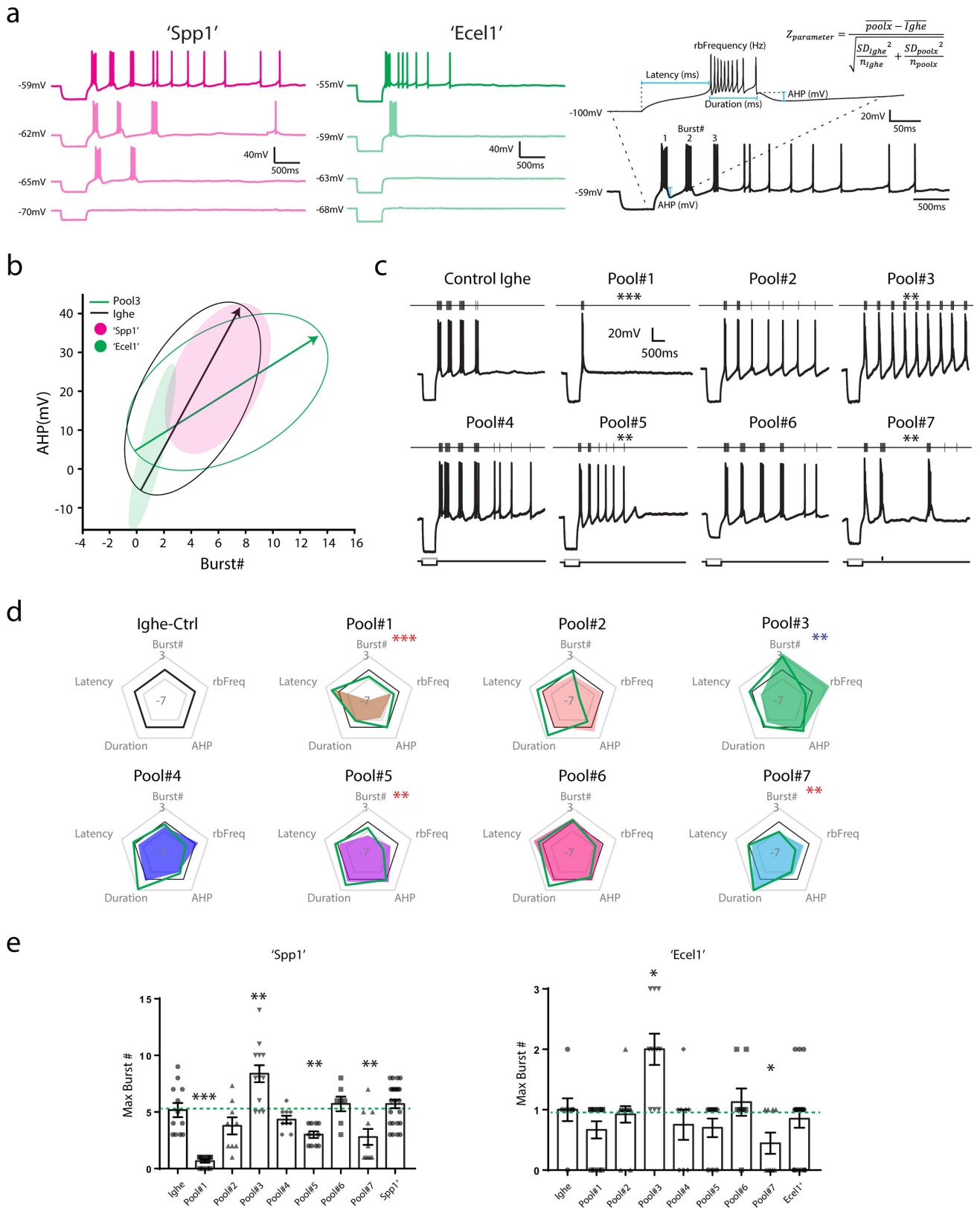
*Risk genes: ASD and Schizophrenia Δ TRN enriched



Extended Data Fig. 7 | AAV-mediated pooled in vivo CRISPR screening.

a, Schematics of the AAV-mediated pooled CRISPR-Cas9 in vivo screen. **b**, List of pools and genes selected for knockout in the CRISPR-Cas9 screening. TRN enriched refers to genes differentially expressed between *Pvalb*⁺ neurons from TRN and from M2 cortex, somatosensory cortex, striatum, and hippocampus. **c**, A heat map showing the expression pattern of the selected genes in the TRN neurons. The selected disease-risk genes are labelled on the right side. **d**, A heat map showing the differentially expressed disease-risk genes in *Spp1*⁺ versus *Ecel1*⁺ neurons: autism spectrum disorder (ASD, purple) and schizophrenia (orange). **e**, Violin plots showing a list of genes differentially expressed between *Pvalb*⁺ neurons in TRN compared and *Pvalb*⁺ neurons in the four other brain regions including hippocampus (HP), secondary motor cortex (M2), somatosensory cortex (SCX), and striatum (STR). **f**, Violin plots confirming the

TRN-enriched gene list as shown in **e** in additional brain regions using the mousebrain.org datasets. CB: cerebellum; Hypoth: hypothalamus; MBd: medial basal nucleus dorsal part; MBV: medial basal nucleus ventral part; SC: spinal cord; Thal: thalamus. **g**, Violin plots showing selected differentially expressed disease-risk genes compared to the *Pvalb*⁺ neurons in the other four brain regions as indicated. HP: hippocampus; M2: secondary motor cortex; SCX: somatosensory cortex; STR: striatum. For **e** and **g**, $n_{HP} = 90$, $n_{M2} = 97$, $n_{SCX} = 116$, $n_{STR} = 13$, $n_{TRN} = 671$ cells; For (**f**), $n_{CA1} = 136$, $n_{CB} = 477$, $n_{Hypoth} = 156$, $n_{MBd} = 331$, $n_{MBV} = 209$, $n_{Medulla} = 121$, $n_{Pons} = 199$, $n_{SC} = 69$, $n_{Thal} = 54$, $n_{TRN} = 501$ cells. The violin plots width is based off of a Gaussian kernel density estimate of the data (estimated by the standard density function in R with default parameters), scaled to have maximum width equal to 1.

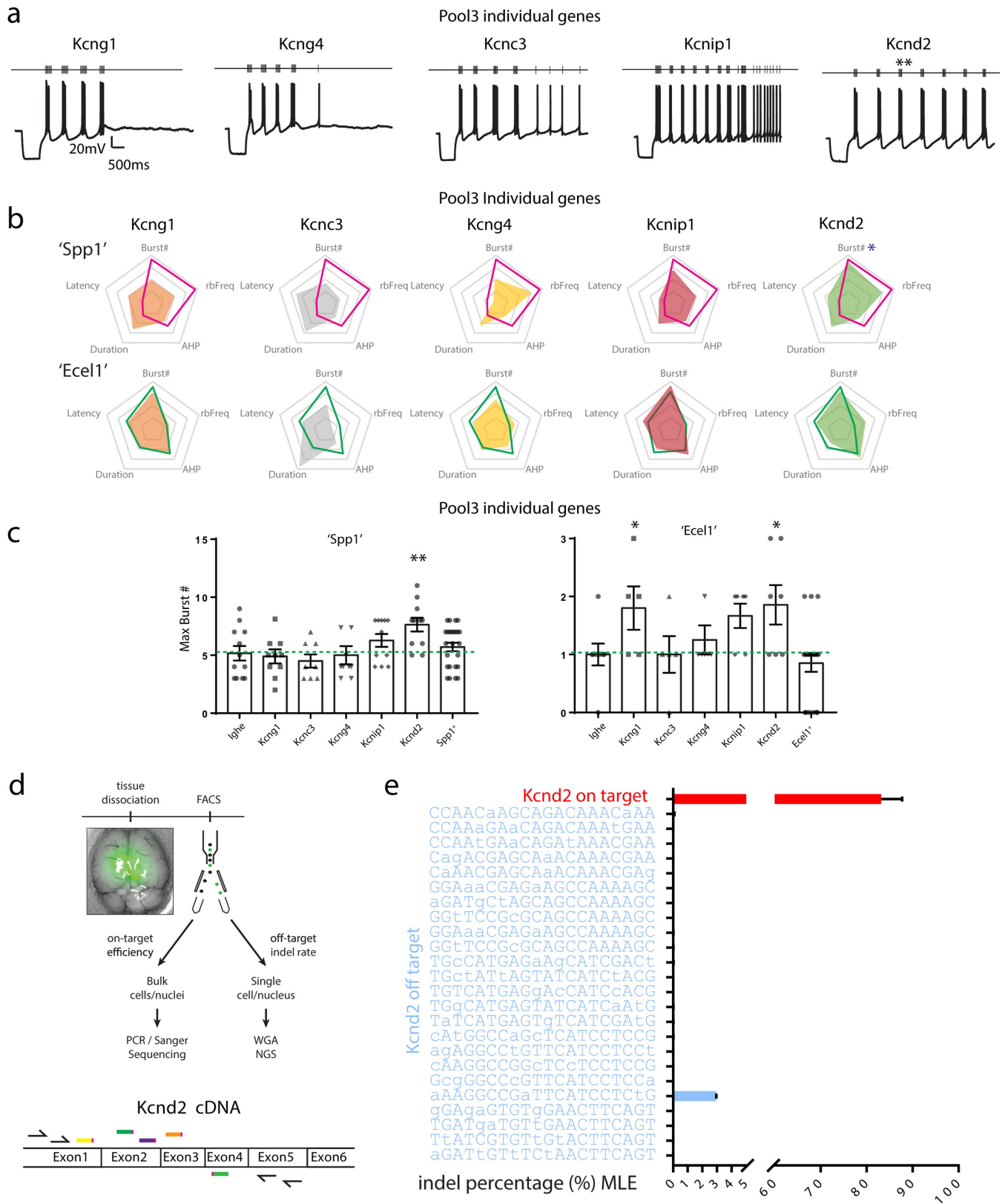


Extended Data Fig. 8 | See next page for caption.

Extended Data Fig. 8 | Pooled in vivo CRISPR-Cas9 screening reveals gene sets contributing to TRN bursting firing properties. **a**, Representative current-clamp recording traces of *Spp1*⁺ like ('Spp1', magenta) and *Ecel1*⁺ like ('Ecel1', green) neurons held at different membrane potentials. The trace with the maximum number of bursts was selected for measuring different burst properties and calculating the Z-score (shown in the right). **b**, Plot showing confidence interval ellipses for classifying *Spp1*⁺ like ('Spp1') and *Ecel1*⁺ like ('Ecel1') neurons based on the AHP and the number of rebound bursts. **c**, Representative rebound burst traces of recorded neurons after knocking out different sets of genes via CRISPR-Cas9 gene editing. Traces show rebound bursting activity changes in response to hyperpolarizing current step injections. TRN neurons exhibited distinct changes in their firing patterns after knockout of different gene groups. **d**, Radar plots of 5 electrophysiological parameters illustrated in **a**, showing the deviation of

perturbed group to the control after knocking out sets of genes in the pooled approach. Positive changes show an increase towards a parameter, while negative changes show a decrease when compared to control. Green line indicates deviations in *Ecel1*⁺ like neurons and colour shades indicates deviations in *Spp1*⁺ like neurons. **e**, Summary of the maximum number of rebound bursts of TRN neurons elicited by comparable hyperpolarizing current step injection as described in Fig. 4b after different sets of genes were knocked out in the pooled approach in *Spp1*⁺ like ('Spp1') vs *Ecel1*⁺ like ('Ecel1') neurons ('Spp1' Pool1, $P = 4.8742 \times 10^{-7}$; Pool3, $P = 0.0033$; Pool5, $P = 0.0088$; Pool7, $P = 0.0065$. 'Ecel1' Pool3, $P = 0.0081$; Pool7, $P = 0.023$, two-sided unpaired *t*-test). Bars represent the mean \pm s.e.m. For **a-e**: 'Spp1' Ighe $n = 12$, Pool1 $n = 12$, Pool2 $n = 9$, Pool3 $n = 13$, Pool4 $n = 9$, Pool5 $n = 10$, Pool6 $n = 9$, and Pool7 $n = 10$ cells; 'Ecel1' Ighe $n = 9$, Pool1 $n = 12$, Pool2 $n = 13$, Pool3 $n = 10$, Pool4 $n = 8$, Pool5 $n = 10$, Pool6 $n = 8$, and Pool7 $n = 9$ cells from 24 mice (3 mice per pool).

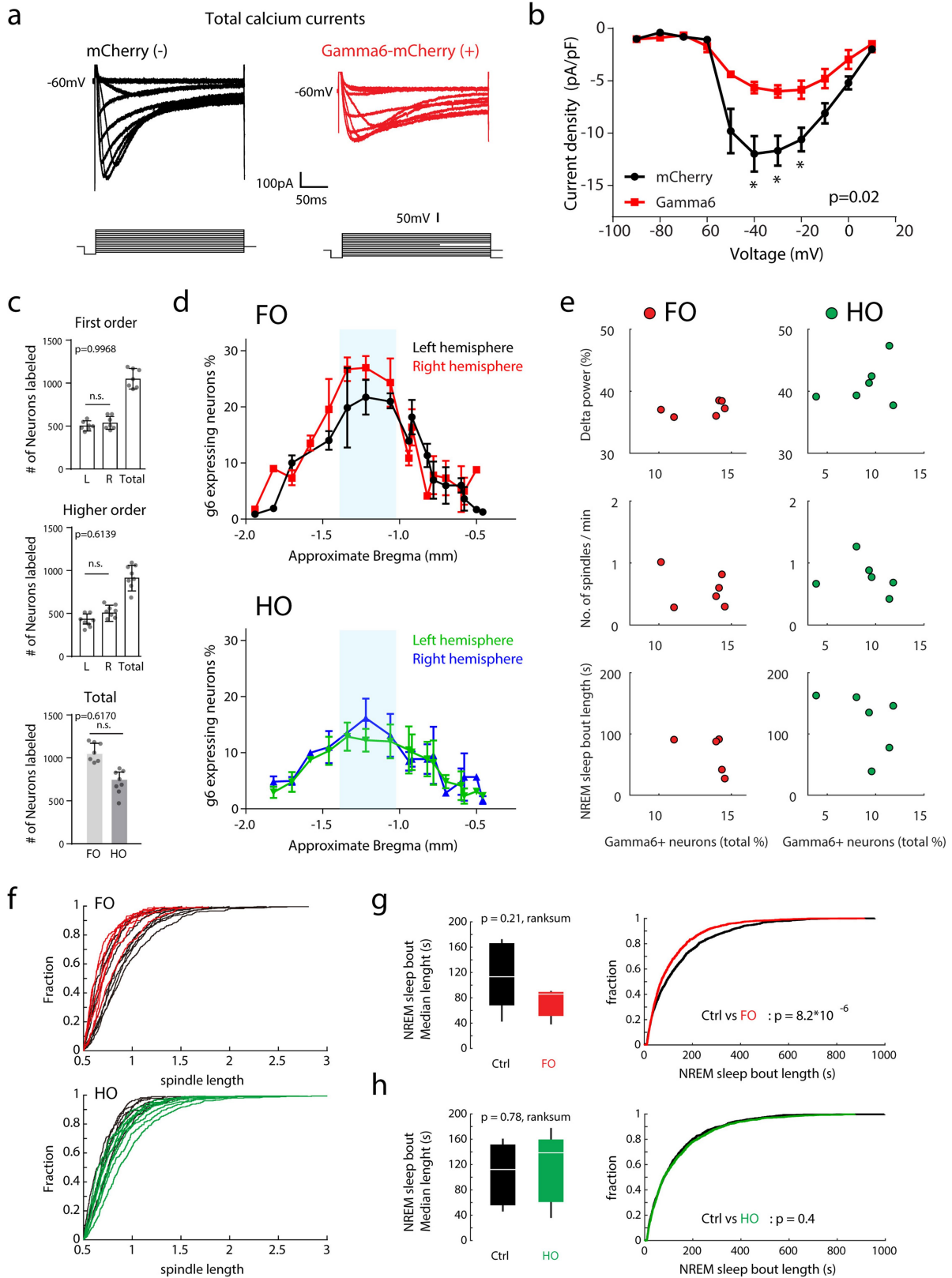
Article



Extended Data Fig. 9 | See next page for caption.

Extended Data Fig. 9 | Characterization and validation of in vivo CRISPR-Cas9 screening reveals key genes contributing to TRN bursting firing properties. **a**, Representative rebound burst traces of recorded neurons after knocking out different individual genes from Pool3 via CRISPR-Cas9 gene editing. Knocking out of *Kcnd2* recapitulates the effects of Pool#3. **b**, Radar plots for Pool3 individual gene. Top: Changes in *Spp1*⁺ like ('Spp1') neurons, pink line showing the effect of the Pool3 gene knock out and colour shades showing the effect produced by individual gene knock out. Bottom: Changes in *Ecel1*⁺ like ('Ecel1') neurons, green line showing the Pool3 gene radar plot and colour shades showing the changes produced by individual gene knock out. *Kcnd2* knockout closely recapitulates the effect of Pool3 in both populations. **c**, Summary of the maximum number of rebound bursts of TRN neurons elicited by comparable protocols after individual genes from Pool3 were knocked out in *Spp1*⁺ like ('Spp1') vs *Ecel1*⁺ like ('Ecel1') neurons ('Spp1' *Kcnd2*, $P=0.0095$. 'Ecel1' *Kcng1*, $P=0.0088$; *Kcnd2*, $P=0.019$, two-sided unpaired *t*-test). Bars represent the mean \pm s.e.m. For **a-c**, 'Spp1' *Kcng1* $n=6$, *Kcnc3* $n=6$,

Kcng4 $n=5$, *Kcnc1* $n=7$, *Kcnd2* $n=7$; 'Ecel1' *Kcng1* $n=10$, *Kcnc3* $n=8$, *Kcng4* $n=9$, *Kcnc1* $n=11$, *Kcnd2* $n=11$. **d**, Schematics of the analysis for on-target and off-target efficiency. Upper: analysis flowchart. WGA: whole genome amplification; NGS: next generation sequencing. Lower: schematics of sgRNA design and primers for on-target analysis for *Kcnd2* knockout. Five sgRNA were designed in Exon2, Exon3, and Exon4. As the length spanned by the leftmost sgRNA and the rightmost sgRNA exceeds the NGS analysis limit, nested PCR combined with Sanger sequencing was used for on-target efficiency analysis. Primers for the nested PCR are shown as black arrows in Exon1 and Exon5. **e**, Bar chart showing the on-target efficiency (5 sgRNA pooled) analysed by nested PCR and Sanger sequencing (control: $n=96$ nuclei, viral injected: $n=384$ nuclei) and off-target rate for the top predicted (Methods) off-target loci of each sgRNA analysed by NGS ($n=1,600$ cells and 72,000 nuclei). Predicted off-target sequences are shown with mismatched bases in lower case. Bar plots represent maximum likelihood estimation (MLE) and upper Wilson score intervals, no raw data point applicable⁶⁴ (Supplementary Information).



Extended Data Fig. 10 | See next page for caption.

Extended Data Fig. 10 | γ_6 expression and its perturbation effect in the TRN cells. **a**, Calcium currents measured in control (black traces) and with γ_6 expression (red traces). **b**, Summarized current density versus voltage relations showing that γ_6 expressing TRN neurons exhibit smaller calcium current densities than controls ($P=0.02$, two-sided unpaired t -test, data presented as mean \pm s.e.m.). For **a**, **b**, $n=6$ neurons/3 mice. **c**, **d**, Quantification of retrogradely labelled cells (**c**; $P=0.6170$, n.s, not significant, two-sided unpaired t -test) and their percentage of total PV⁺ neurons (**d**) in the series of coronal slices from injected mice. L: left hemisphere; R: right hemisphere; g6: γ_6 ; FO: first order; HO: higher order. For **c**, **d**, $n=7$ for each experimental condition, data presented as mean \pm s.e.m. For **c**, plots are overlaid with raw data points. **e**, Scatter plots showing γ_6 expressing percentage and the effect

size for individual mice. Top row: delta power percentage; middle row: number of spindles per minutes in NREM; bottom row: median length of sleep bout in NREM in seconds; dots: animals with retrograde γ_6 injection in FO (Red) and HO (Green) somatosensory thalamic nucleus. $n=6$ for each conditions. **f**, Cumulative distribution of sleep spindle length for each individual mouse with retrograde γ_6 injection in FO (upper) and HO (lower) somatosensory thalamic nuclei, corresponding to Fig. 5h. **g**, **h**, Summary of median length of NREM sleep bouts with retrograde γ_6 injection in FO (**g**) and HO (**h**) somatosensory thalamic nuclei. Right: two-sided Wilcoxon rank-sum test; Left: Kolmogorov-Smirnov test. For data in **f**-**h**, n_{control} (FO) = 8, n_{γ_6} (FO) = 8, n_{control} (HO) = 7, n_{γ_6} (HO) = 8. Box plots represent minima, 25th, 50th, 75th percentiles, maxima.